Identification of novel factors involved in polarized cell expansion and development in the moss, *Physcomitrium patens*

コケ植物 *Physcomitrium patens* における極性細胞の伸長と発生に関与する新規因子の同定

A

DISSERTATION

Submitted to the Graduate School of Life Science,

Hokkaido University

In partial fulfillment of the requirement for the degree of

DOCTOR OF LIFE SCIENCE

By

PRERNA SINGH

MAR 2025

Contents

Abstract

Tip growth is vital for plant growth and development, yet the regulatory mechanisms governing this process remain incompletely understood. In this study, I identified Reagent F4, a novel small molecule that disrupts tip growth and polarized cell expansion in the moss, *Physcomitrium patens* protonemata. Through unbiased chemical screening, I found that Reagent F4 induces abnormal protonemal morphology, characterized by reduced cell elongation and stunted cell expansion. My analyses revealed that F4 treatment triggers actin depolymerization and disrupts apical actin foci, which are critical for initiating and maintaining tip growth. Additionally, both acute and prolonged F4 exposure led to mislocalization of ROP GTPase, a key regulator of cell polarity. Transcriptomic analyses of F4 treated protonemata show significant downregulation of genes involved in lipid asymmetry, a process essential for polarized growth. These findings establish Reagent F4 as a valuable tool to investigate the molecular mechanisms governing tip growth in *P. patens* and highlight the potential role of lipid asymmetry in coordinating cytoskeletal organization and membrane polarity.

Introduction

In multicellular eukaryotes, cell polarity is crucial for various cellular, tissue, and organism-level functions and physiology, including responses to the external environment. These properties are significant for developmental processes, such as establishing the body plan and forming organizational systems (Gorelova et al., 2021; Guo and Dong, 2022). The establishment and maintenance of cell polarity represent a highly conserved and intricate mechanism that relies on the precise delivery of intracellular signals and materials. The establishment of cell polarity is essential for conferring specialized functions to various cell types. For example, the polar localization of auxin transporters, such as PIN-FORMED (PIN) proteins, drives the polar movement of auxin within various tissues in *Arabidopsis thaliana* (Michniewicz et al., 2007); the polar localization of BOR1 facilitates the polar transport of boron in the endodermis of roots (Takano et al., 2010). Additionally, transient polar localization of BASL protein facilitates asymmetric cell division of stomatal-lineage cells (Dong et al., 2009). Root hairs, pollen tubes in seed plants, and protonemal filaments in mosses extend through a process called tip growth. This growth requires a polarized intracellular organization that delivers cell membrane and cell wall materials to the apical region, thereby sustaining polarized cell growth (Hepler et al., 2001).

The moss, *Physcomitrium patens,* is an excellent model plant to study mechanisms of tip growth in plants; *P. patens* spends a majority of its gametophytic life stage in the juvenile, protonemal form, where the protonemata display distinct unidirectional and anisotropic growth patterns by undergoing tip growth via polarized cell expansion and asymmetric cell division (Menand et al., 2007; Naramoto et al., 2022; Rensing et al., 2020). Actin is vital for tip growth in bryophytes like *P. patens* (Augustine et al., 2008). Pharmacological inhibition of actin cytoskeleton or mutants defective in the function of actin-binding proteins (Augustine et al., 2008; Vidali et al., 2007) or actin nucleating factors (Vidali et al., 2009) exhibit a loss of polarized growth. Another cytoskeletal component, microtubules,

help in establishing the tip growth direction in *P. patens* (Yamada and Goshima, 2018), while also intersecting with the polarization of actin clusters in the apical cells, facilitated by myosin VIII and kinesin proteins (Wu and Bezanilla, 2018a; Yamada and Goshima, 2018). Furthermore, polarized growth is also influenced by exocytosis and specific cell wall components along with their modifications (Ye and Zhong, 2022). One of the key signaling molecules involved in regulating cell growth and polarization in tip-growing cells of moss protonemata is the CDC42/RHO/RAC-like small GTPases known as RHO-related GTPases of plants (ROPs). In *P. patens protonema*, ROP polarizes in a compact apical gradient in the plasma membrane of tip-growing cells (Cheng et al., 2020; Ito et al., 2014; Yi and Goshima, 2020). Loss-of-function mutants of ROPs and their effectors compromise polarized tip growth in *P. patens* (Burkart et al., 2015; Cheng et al., 2020; Yi and Goshima, 2020). The polarized distribution of ROP is mediated through interactions with lipids facilitated by the polybasic hypervariable region and a carboxyl-terminal CAAX prenylation motif. While the importance of the prenylation signal in the proper localization of ROP is known (Yi and Goshima, 2020), the mechanisms underlying ROP-membrane interaction in *P. patens* are not fully understood.

Over the last two decades, classical genetics has served as the primary means to unravel the mechanisms underlying cell polarity (Dong et al., 2009; Müller et al., 1998; Takano et al., 2010). Although this approach has yielded valuable insights, it has limitations. For instance, plant genomes often exhibit high genetic redundancy, resulting in loss-of-function mutants displaying phenotypes similar to the wild type (Borevitz and Ecker, 2004). Additionally, creating a complete collection of loss-of-function mutants for essential genes may lead to lethality. Both redundancy and lethality are frequently encountered in genes that regulate essential cellular functions. Chemical genetics offers a promising alternative to address these challenges (Schreiber, 1998). The cellular responses can be finely tuned by applying small molecules in a spatially and temporally controlled manner. In this study, I employed a novel chemical called F4 to explore the mechanisms

behind polarized cell expansion in the moss *P. patens*. The reagent F4 disrupts actin organization and leads to a loss of apical localization of ROP small GTPases. The unique structure of this compound suggests that F4 may interact with novel components or pathways related to cell polarity. Additionally, transcriptome analyses indicate that Reagent F4 might be involved in the maintenance of lipid asymmetry via flippase activity. Thus, I propose the novel chemical Reagent F4 to investigate new aspects of lipid asymmetry in coordinating cytoskeletal organization and membrane polarity.

Materials and Methods

Plant materials and growth

The moss *Physcomitrium patens* Bruch & Schimp subsp. *patens* was used as the wild-type (WT) strain in this study (Ashton and Cove, 1977; Rensing et al., 2020). LifeAct-Venus, a marker for actin filaments (Era et al., 2009) , and GFP-Tubulin, a marker for microtubules(Hiwatashi et al., 2008), were employed to visualize the cytoskeleton. ROP4swmNG was utilized as a marker for ROP GTPases in *P. patens* (Cheng et al., 2020). Wild-type (WT) and transgenic marker lines were homogenized in sterile water and plated on BCDAT or BCD with 0.8% (w/v) agar medium. Cultures were maintained under continuous white light (*c.* 25 lmol photon m^{-2} s^{-1}) at 25°C (Nishiyama et al., 2000). Protonemal tissues from 4- to 5-day-old subcultures were utilized for subsequent experiments. For the inducible system, β-estradiol (Wako, Osaka, Japan) was added to a final concentration of 10 nM to 5-day-old protonemal tissues cultured in 35-mm Petri dishes with a 27-mm glass coverslip at the bottom (Iwaki, Japan) containing 500 μL of BCD with 0.8% (w/v) agar and used for observation subsequently.

Chemical screening

For screening as well as structure-activity relationship (SAR) analysis (McKinney et al. 2000), WT protonemal tissues were inoculated into 96-well plates with glass coverslip bottom (Iwaki, Japan), each containing 80 μl of BCDAT medium supplemented with 0.5% (w/v) glucose (BCDATG) and 0.5% (w/v) gellan gum (Wako, Japan). The plates were incubated upside down under red light (*ca*. 27 μmol photon m^{-2} s^{-1}) to suppress side branch formation at 25°C for 5 days. Screening for small molecules that induce defects in tip growth and/or cell expansion was conducted using the chemical library provided by ITbM, Nagoya University, which consisted of 2,000 compounds dissolved in DMSO at a stock concentration of 10 mM. For the chemical screening experiments, the compounds were diluted in liquid BCDAT medium containing 0.5% (w/v) glucose (BCDATG) to a

working concentration of 100 μM. Following the 5-day incubation of WT samples under red light, the diluted small molecules were added to the wells to a final concentration of 10 μM. Samples were then incubated for another 2 days under continuous white light, with 0.1% (v/v) DMSO as the negative control. Observations were conducted every 24 hours over the 2-day treatment period using a fluorescence microscope (Olympus BX60). For SAR analysis, Reagent F4 analogs were dissolved in DMSO at a stock concentration of 10 mM, then diluted in liquid BCDATG. The diluted solutions were added to wells to achieve a final concentration of 100 μM, with 100 μM Reagent F4 as a positive control and 0.1% (v/v) DMSO as a negative control. Higher concentrations of compounds were used for SAR analysis to ensure a clear phenotype, compared to those used in chemical library screening.

Microscopy

To assess the dose-dependent effects of Reagent F4 and conduct the structure-activity relationship (SAR) assay, subapical cell lengths of protonemal tissues were measured using an Olympus fluorescence microscope with a 10× objective. For live imaging of cytoskeletal elements and ROP under the influence of Reagent F4, protonemal cells were cultured in 35-mm Petri dishes with a 27-mm glass coverslip at the bottom (Iwaki, Japan). The culture medium consisted of 500 μL of BCD with 0.8% (w/v) agar or BCDATG with 0.5% (w/v) gellan gum (Wako, Osaka, Japan) and samples were grown under continuous white light and red light respectively, for 5–7 days. Reagent F4 and DMSO were diluted in liquid BCD/BCDATG and applied exogenously to final concentrations of 100 μM and 0.1%, respectively. Latrunculin B and Oryzalin were also diluted in liquid BCD and applied exogenously to final concentrations of 1 μM and 10 μM, respectively. Cytoskeletal elements (LifeAct-Venus, GFP-Tubulin) and ROP (ROP4swmNG) were visualized using an inverted spinning disk confocal microscope (X-Light V3, CrestOptics) equipped with a 1.40 NA 60× oil immersion objective (Plan Apo VC 60X, Nikon). Fluorescent markers were excited using a 470 nm laser, while

chlorophyll autofluorescence was excited with a 640 nm laser. Emission filters were set to 485–535 nm for GFP and 660–735 nm for chlorophyll. Image acquisition was managed via MetaMorph software (Molecular Devices). mCherry-HDEL (ER marker), LifeAct-mCherry in pGX8Y-PpAPL5 background, were observed using a Zeiss LSM 980 laser-scanning confocal microscope with a Plan Apochromat 63×/1.40 oil immersion objective. Emission filters were set to 485–535 nm for GFP, 552nm – 610nm for mCherry and 660–735 nm for chlorophyll. Quantification of filament density (amount of cytoskeletal components per unit area in specific cell regions) and skewness (statistical parameter that quantifies fluorescence distribution asymmetry where normal cytoskeletal filaments exhibit a normal distribution of fluorescence intensities and an increase in brighter pixels from bundling shifts, leading to higher skewness values) was done as described by (Higaki, 2017), and normalized mean intensity graphs of ROP apical gradient were generated by measuring the signal intensity along a manually drawn line tracing the plasma membrane of the apical cell starting from the left lateral side of the cell to the right lateral side of the cell as described in (Cheng et al., 2020). All microscopy data analyses were performed using Fiji (ImageJ) software (Schindelin et al., 2012).

FRAP Assay

Apical cells in samples grown in BCDATG (0.5% (w/v) glucose supplemented with 0.5% (w/v) gellan gum) under red light for 5–6 days were observed using a Zeiss LSM 980 laser-scanning confocal microscope with a Plan Apochromat 63×/1.40 oil immersion objective. A circular stimulation ROI with a diameter of 3 μm was placed at the apical plasma membrane where the ROP signal was the strongest. The 488 nm laser at 100% power was used for stimulation. Before stimulation, images were taken every 2 s for 10 s, followed by stimulation for 2 s, and the imaging continued after stimulation every 2 s for a total of 1.5 min. The mean fluorescence intensity of the ROP4swmNG signal was measured

within the stimulation ROI. For each cell, the mean intensity measurements for the first five time points before stimulation were averaged to generate the reference intensity, and the mean intensity value of every time point in the whole movie was divided by the reference intensity value to create a normalized mean intensity. Graphs were generated by averaging each cell's normalized mean intensity and plotting versus time. Photobleaching of the apical cell was started 30 minutes after exogenous application of the compound and the control.

RNA sequencing

Total RNA was extracted from protonemal tissues treated with 100 µM Reagent F4 using the RNeasy Plant Mini Kit (Qiagen). Tissues were collected at 1, 3, 12, and 24 hours after treatment. Protonemata treated with 0.1% (v/v) DMSO served as the control. Three technical replicates were sampled for each treatment and time point. Following RNA quality assessment, sequencing libraries were prepared using the Lazy-Seq protocol (Kamitani et al., 2019). High-throughput RNA sequencing was conducted on the NovaSeqX Plus platform (Illumina) in 150-bp paired-end mode.

RNA sequencing analysis

After sequencing, raw data were obtained in FASTQ format, and data quality was assessed using FastQC (Andrews S, 2010) and MultiQC (Ewels et al., 2016). Read trimming was performed with Cutadapt (Martin, 2011). Transcript abundances were quantified using Kallisto (Bray et al., 2016) by aligning the reads to the *Physcomitrium patens* genome v3.3, obtained from Phytozome (https://phytozome-next.jgi.doe.gov/). Transcript abundance estimates were imported and summarized using the *tximport* package (Soneson et al., 2016), followed by differential gene expression analysis conducted with DESeq2 (Love et al., 2014). All analyses were performed on the Galaxy platform (Afgan et al., 2016). Subsequent hierarchical clustering of normalized counts and Gene Ontology (GO) term enrichment analysis were carried out using iDEP 2.0 (Ge et al., 2018) and ShinyGO 0.81(Ge et al., 2020). Hierarchical clustering was done with the Euclidean distance measure

with complete linkage, and values were plotted as TPM values. Time-course clustering of the DEGs was conducted by the Mfuzz package and plotted using SRplot (Tang et al., 2023).

DARTS assay

The DARTS assays for identifying and validating potential protein interactors of Reagent F4 were performed as previously described (Lomenick et al., 2009), with some modifications. For unbiased target identification, 5-day-old wild-type (WT) protonemata grown on BCDAT agar media were utilized for total protein extraction. All extraction steps were conducted at 4°C. After harvesting, 0.2 g of protonemal tissue was ground to a fine powder in liquid nitrogen and resuspended in 1 mL of freshly prepared total protein NETN extraction buffer (10 mM Tris-HCl [pH 8.0], 100 mM NaCl, 500 µM EDTA, 0.5% [v/v] NP-40) containing 2 mM DTT, 1% Triton X-100, 1 mM PMSF, 1X cOmplete protease inhibitor cocktail (Roche 11836170001), and phosphatase inhibitors (25 mM sodium fluoride, 20 mM sodium pyrophosphate, 10 mM β-glycerophosphate, and 2 mM sodium orthovanadate). The homogenate was then centrifuged at 20,000 g for 5 minutes to remove cell debris. After determining the protein concentration using Bradford protein concentration assay reagent (Biorad 5000205), the protein extract, at a concentration of 4.8 mg/mL, was divided into three 1.5 mL Eppendorf tubes. Each was incubated with Reagent F4 at concentrations of 100 µM, 200 µM, or an equal volume of DMSO (1% [v/v]) as a mock control, for 1 hour at room temperature with slow mixing. The treated protein extracts were further aliquoted, and each aliquot was mixed with Pronase (Roche) (10 mg/mL stock solution) at corresponding dilutions to achieve targeted enzyme-to-protein substrate ratios of 1:100, 1:300, and no Pronase. After incubation at room temperature for 30 minutes, proteolytic digestion was halted by adding 20X cOmplete protease inhibitor cocktail (Roche), and the tubes were placed on ice immediately. The DARTS protein samples were denatured and reduced in a denaturing buffer (6 M Guanidin-HCl, 0.1 M

Tris-HCl [pH 8.0], and 5 mM EDTA [pH 8.0]) containing 0.3% (w/v) DTT at 20°C for 1 hour. For nanoLC-MS/MS analysis, all subsequent steps were performed on-column using Vivacon 500 10K Spin Columns (Sartorius Stedim VN01H01). The samples were further alkylated in the alkylation buffer (10 mM iodoacetamide in the denaturing buffer) at room temperature for 30 minutes in the dark and digested with trypsin (Promega V5280) at a 1:100 (w:w) enzyme-to-sample ratio in 50 mM ammonium bicarbonate at 37°C overnight in the dark with gentle rotation. After centrifugation, the flow-through containing the tryptic peptides was treated with 0.1% formic acid to stop digestion and collected for LC-MS/MS analysis. Additionally, aliquots of the DARTS protein samples were mixed with protein loading buffer (10% SDS, 500 mM DTT, 50% glycerol, 500 mM Tris-HCl, 0.05% bromophenol blue) and denatured at 70°C for 5 minutes prior to electrophoresis. The gel was stained using a silver staining kit (Atto 2332360) following the vendor's protocol and visualized with a Fujifilm LAS-300 imager. For the validation of Reagent F4's binding to PpAPL5-Citrine, the compound-treated protein extracts were divided into aliquots, and different dilutions of Pronase—1:100, 1:300, and no Pronase—were added for a 30-minute digestion at room temperature. The samples were then mixed with a protein loading buffer and boiled at 70°C for 10 minutes to stop the proteolytic reaction. For immunodetection, the proteins were resolved on 12% SDS-PAGE acrylamide gels and immunoblotted using mouse monoclonal anti-GFP JL-8 (Clontech, dilution 1:1,000) and anti-mouse IgG (GE Healthcare, dilution 1:4,000). Blots were developed with Amersham™ ECL™ Prime Western Blotting Detection Reagent (Cytiva RPN2232) and imaged using the Fujifilm LAS-300 Imager.

Mass spectrometry analysis

DARTS protein samples were trypsin digested and prepared for mass spectrometry. The peptides were analyzed by Thermo Scientific LTQ-OrbitrapXL mass spectrometer. For quantitative comparison of protein and peptide abundances, MS spectra were analyzed

using MaxQuant(Cox et al., 2014; Smaczniak et al., 2012). Raw data files in thermo.raw format were uploaded into the MaxQuant software. The chemical modifications occurring due to preparation procedures parameters were set as per the default settings and "Heavy-labels" was unselected. A *P. patens* protein database obtained from UniProt (Proteome ID: UP000006727) was used as the reference database. "Match between runs" and "LFQ" parameters were selected before running the analysis. The protein and peptide abundances (Intensity) obtained were used for calculating the fold change by dividing the 100 µM F4 (1:100 Pronase) intensity values by the DMSO (1:100 Pronase) intensity values.

Molecular cloning and transgenic plants

To generate PpAPL5-Citrine inducible construct, coding sequences were PCR-amplified using PrimeSTAR Max DNA polymerase (Takara, Japan) and cloned into pENTR1A (ThermoFisher) and sequenced, before being subcloned into pGX8Y (Kubo et al., 2013) using LR reactions to generate pGX8Y-PpAPL5. Similarly, to generate pGX8-mCherry-HDEL inducible construct, sequences including N-terminal signal peptide (SP), mCherry tag and a C-terminal attached ER retention signal, His-Asp-Glu-Leu (HDEL) were PCR-amplified using PrimeSTAR Max DNA polymerase (Takara) from pGWB701-UBQ10-mCherry-HDEL plasmid provided by Takagi Junpei at Hokkaido University. The amplified sequence was cloned into pENTR1A (ThermoFisher) and sequenced, before being subcloned into a modified pGX8 with zeocin antibiotic cassette (Kubo et al., 2013) using LR reactions to generate pGX8-mCherry-HDEL : Zeocin. The list of primers used for this plasmid construction is listed in Table S2.

To generate transgenic moss, protoplasts of appropriate genetic background were prepared and transformed with 15 µg of plasmid DNA. The polyethylene glycol (PEG)- mediated transformation was performed as described previously (Nishiyama et al., 2000). The final transgenic lines of pGX8Y-PpAPL5 in WT background and pGX8Y-PpAPL5 in mCherry-HDEL background were selected twice on BCDAT agar medium containing

30 mg/L hygromycin B (Wako), and pGX8-mCherry-HDEL in WT background and pT1OG-LifeAct-mCherry in the PpAPL5iOx-Citrine background were selected twice on BCDAT agar medium containing 50 mg/L zeocin (Invitrogen).

Gene identifiers, phylogenetic tree construction and bioinformatics

APL amino acid sequences and respective gene identifiers were retrieved from Phytozome v13 (https://phytozome-next.jgi.doe.gov). These sequences were aligned with MAFFT https://www.ebi.ac.uk/jdispatcher/msa/mafft (Madeira et al., 2024). Gaps between sequences were removed using Jalview (Waterhouse et al., 2009). Maximum likelihood analysis of the amino acid sequences was then performed using the MEGA 11 software (Tamura et al., 2021) by choosing Jones-Taylor-Thornton (JTT) substitution model and standard bootstrap analysis, with 1000 bootstrap alignments. The following web tools were used to predict the presence of signal peptide (SignalIP-5.0,http://www.cbs.dtu.dk/services/SignalP/), and other domains, InterProScan5 (https://www.ebi.ac.uk/interpro/search/sequence/). Web-based Illustrator for Biological Sequences (IBS, https://ibs.renlab.org/#/home) was used to draw schematic representations for genes and proteins (Liu et al., 2015).

Statistical analysis

One-way ANOVA with Tukey's post-hoc test was performed using GraphPad Prism version 10.4.1 for Windows, GraphPad Software, www.graphpad.com. Details about the statistically significant differences are described in the figure legends.

Results

CHAPTER I: IDENTIFICATION OF A NEW CHEMICAL AND ITS MECHANISM OF ACTION THROUGH TRANSCRIPTOMICS

Identification of small molecules that affect tip growth in P. patens

To identify novel factors that affect tip growth and polarized cell expansion in *P. patens* protonemata, I established a chemical screening method utilizing an unbiased chemical library of 2000 chemical compounds provided by ITbM. The screening aimed to identify compounds that induced aberrant protonemal morphologies, using dimethyl sulfoxide (DMSO) as a negative control. Wild-type (WT) protonemata were cultured in 96-well plates under red light for 5 days, then treated with compounds at a final concentration of 10 µM, and finally cultured under white light for two additional days (Fig 1A). This led to the identification of a [1,3,4] thiadiazole derivative, 6-(2,3-dihydro-1,4-benzodioxin-6-yl)-3-(3-pyridinyl) - [1,2,4] triazolo[3,4-b] [1,3,4] thiadiazole, referred to as "Reagent F4" (Fig 1B). Application of Reagent F4 resulted in a marked reduction in cell length and swollen cells with stunted cell expansion of protonemata (Fig 1C). With no prior biological activity reported for Reagent F4, my results suggest that it might act as an inhibitor of polarized growth in *P. patens* protonemata, potentially through mechanisms that are novel and yet to be characterized.

Reagent F4 inhibits cell elongation in P. patens

To comprehensively evaluate the effects of Reagent F4, I specifically examined its impact on the morphology of protonemata, focusing on the length of subapical cells. Subapical cells, which are positioned below the apical cells in the protonemal structure, undergo minimal expansion following cell division. This characteristic, in contrast to the more

dynamic cellular behavior seen in apical cells, makes subapical cells a more reliable metric for assessing the influence of compounds on cell expansion.

A clear dose-dependent reduction in the length of subapical cells was observed in protonemata treated with Reagent F4. Specifically, as the concentration of Reagent F4 increased, I noted a corresponding decrease in the length of the subapical cells, strongly indicating that this reagent acts as an inhibitor of cell expansion (Fig. 2A, B).

In addition to assessing the morphological impacts, I aimed to pinpoint the specific molecular structure responsible for the observed biological activity of Reagent F4. To achieve this, I conducted a structure-activity relationship (SAR) analysis using five analogs of Reagent F4. I aimed to identify F4 analogs that induced phenotypes similar to F4, upon application to *P. patens* protonema. Through this analysis, I identified compounds E6 and F4' that showed a reduction in the subapical cell length, a phenotype also observed upon Reagent F4 treatment (Figure 2C, D). Since Reagent F4, E6, and F4' share common moieties consisting of two heteroaromatic rings in their chemical structures, I conclude that these heteroaromatic rings are likely essential for the biological activity of Reagent F4 (marked in blue, Figure 2C). Although compounds E6 and F4' phenocopy Reagent F4's effect on *P. patens* protonema, the reduction of subapical cell length is not as strong as that observed in samples treated with F4. The chemical structures of F4, E6, and F4' differ in their -R group (marked in pink, Figure 2C). The difference in the intensity of the phenotype induced by the compounds and the difference in the -R group suggests that the -R group attached to the core structure might play a role in modulating the intensity of the chemical's effects (Figure 2D).

Reagent F4 treatment leads to actin depolymerization and loss of actin foci

Due to the defective cell elongation and tip growth phenotypes upon Reagent F4 treatment, I sought to explore whether alterations in the organization of cytoskeletal elements were the

underlying mechanism driving these physiological changes in cell shape and size. The cytoskeletal elements were observed by utilizing LifeAct-Venus transgenic line for actin filaments and GFP-Tubulin transgenic line for microtubules. My observations indicated that even an acute exposure of approximately two hours to Reagent F4 resulted in a significant reduction in the overall density of actin filaments within the protonemata (Figure 3A, B). Notably, F4 treatment, like latrunculin B (LatB), an actin polymerization inhibitor, appeared to promote actin bundling, resulting in persistent, bright, long cable-like filaments (Figure 3A, C). This suggests that the treatment induces actin network depolymerization. Interestingly, acute exposure to Reagent F4 did not induce noticeable disorganization of the microtubule network, unlike the effects observed with oryzalin treatment (Figure 4). This suggests that the primary impact of Reagent F4 on polarized cell expansion is likely mediated through its specific effects on the actin cytoskeleton, rather than through disruption of the microtubule network. Previous studies have also reported defective actin filament organization leading to stunted cell elongation and perturbed tip growth in moss (Augustine et al., 2011; Harries et al., 2005; Vidali et al., 2007), indicating the importance of actin filaments in tip growth of *P. patens* protonemata.

At the tip of protonemal apical cells, dense F-actin filaments accumulate into spot-like structures (Finka et al., 2007), termed as foci. These foci predict the sites of cell expansion (Wu and Bezanilla, 2018b) and help establish polarized cell expansion. Under the effect of Reagent F4, the actin foci in most of the apical cells were lost over the course of an hour (n = 17/19, Figure 3D). These observations suggest that Reagent F4 impedes tip growth by perturbing the organization of the actin cytoskeleton.

Reagent F4 affects ROP polar localization

In the protonema of *P. patens*, ROP displays a compact apical gradient in the plasma membrane of the apical cells (Cheng et al., 2020; Yi and Goshima, 2020). My observations

above noted a loss of tip growth, prompting me to investigate how Reagent F4 impacts this important polarity regulator, ROP.

In actively growing tip cells, the apical gradient of ROP is maintained. However, acute treatment with Reagent F4 resulted in the loss of this gradient in approximately 73% of the observed apical cells (n = 29/40) as opposed to the mock samples that did not exhibit a complete loss of ROP gradient (Figure 5A). Notably, this disappearance occurs within 30 minutes of Reagent F4 application, resembling the previously reported effects of Lat B on the ROP gradient (Figure 3A, Cheng et al., 2020). Considering the underlying cause for the loss of the ROP apical gradient, I sought to determine whether Reagent F4 influences ROP dynamics at the cell apex. To investigate this, I employed fluorescence recovery after photobleaching (FRAP) to assess the ROP signal's mobility following 30 minutes of Reagent F4 treatment. My results showed that Reagent F4 did not significantly alter the recovery of the ROP signal; both control and treated samples exhibited similar recovery times, approximately 40 seconds (Figure 5B, Supplemental Movie 1).

ROP is also essential for branch formation, as it accumulates at the sites of side branch initiation along the lateral wall. Notably, ROP predicts future side branch formation by localizing to the apicolateral portion of subapical cells several hours before the protrusions occur (Cheng et al., 2020). To further investigate whether F4 treatment affects ROP localization along the lateral walls, I examined ROP distribution in protonemata after longer exposure to F4. While prolonged exposure to F4 diminished ROP localization at the tips of some apical cells, we observed ectopic ROP localization in several cells (Figure 5D-G). For instance, after extended treatment of F4 for 24 hours, ROP accumulated on the lateral sides of apical cells (Figure 5D), and aberrantly at the medial side of both subapical and third cells (Figure 5E). Additionally, basal ROP accumulation was noted in subapical cells (Figure 5F), indicating potential side branch formation from unusual middle or basal regions. Consistently, some cells displayed abnormal side branch protrusions from the

406 medial region of subapical cells (Figure 5G), where ROP was correctly localized at the tips
407 of these protrusions. These findings suggest that F4 treatment disrupts ROP localization
408 along the lateral wall, resulting in abnormal side branch formation at atypical positions.
409 Hence, my results indicate that while Reagent F4 does not alter ROP dynamics, it may lead
410 to the loss of ROP signaling due to specific spatial changes in ROP localization.

411

412 *Identification of Reagent F4's mechanism of action through transcriptomics*

413 Since physiological changes were observed under both acute and sustained, long-term
414 influence of Reagent F4, I wanted to identify the underlying factors corresponding to the
415 physiological changes brought about by exposure to Reagent F4. To better understand the
416 transcriptional landscape upon Reagent F4 application, RNA sequencing analyses were
417 performed with WT protonemata treated with 100 µM Reagent F4 at 4 different time points
418 (1 hour, 3 hours, 12 hours, 24 hours), with 0.1% DMSO as a mock control. Differential
419 gene expression analyses were carried out with DESeq2 and filtered for genes with adjusted
420 *p-value* < 0.05 and absolute log2FC value > 0.58. The reproducibility of the experimental
421 data was confirmed by principal component analysis, showing distinct expression patterns
422 of Reagent F4 treated samples, compared to the mock samples (Figure 7A). The similarities
423 between the individual biological replicates demonstrate the high reproducibility of the
424 measurements. Hierarchical clustering of normalized counts of the most differentially
425 expressed genes (DEGs) revealed a significant shift in the transcriptome after just one hour
426 of acute F4 treatment (Figure 6A). Additionally, replicates clustered together at 12 and 24
427 hours, indicating similar expression patterns at these time points. Compared to mock
428 samples, samples treated with Reagent F4 generated 924 DEGs across all time points. I
429 identified the highest number of DEGs at 12 hours after F4 treatment, and 241 genes
430 showed common changes across all F4 chemical treatments (Figure 6B, Table S1).

Among the upregulated DEGs, cyclin-dependent kinase activity (GO:0016538, GO:0019207, GO:0019887) -related GO terms were significantly enriched in the upregulated DEGs (Figure 6C). Though I did not observe any significant transcriptional changes of PpCDKA1, PpCDKA2, PpCDKB1 or PpCDKB2 (Bao et al., 2022), I found that genes involved in G1-to-S phase transition (CYCD) as well as G2-to-M phase transition (CYCA/CYCB) (Inzé and Veylder, 2006) exhibited increased transcript levels (Table S2). Time-course clustering of the DEGs suggests a steady upregulation of cell cycle-related genes from 1 hour F4 treatment onwards and continued to be upregulated post 12 hours F4 treatment (Figure 8, Cluster 2). This indicates that Reagent F4 might influence cell cycle-related genes in *P. patens* protonemata, although any phenotypes substantiating this hypothesis have not been observed yet.

Gene ontology (GO) enrichment analysis (Table S2) of the downregulated DEGs showed that the GO Molecular Functions, glycerophosphodiester phosphodiesterase activity (GO:0008889), intramembrane lipid transporter activity (GO:0140303, GO:0140326), sensory histidine kinase activity (GO:0000155, GO:0004673, GO:0016775), and serine/threonine kinase activity (GO:0004674, GO:0004672) - related GO terms were highly enriched (adjusted FDR $P \leq 0.05$) (Figure 6D). The downregulated DEGs clustered separately based on the time-course coregulation. Glycerophosphodiester phosphodiesterase activity-related (GO:0008889) and intramembrane lipid transporter activity-related (GO:0140303, GO:0140326) GO terms clustered together showing a steep downregulation just 1 hour post F4 treatment (Figure 8, Cluster 7). This downregulation continued up to 12 hours of F4 treatment, after which a slight upregulation is observed, although it does not reach the mock samples' transcript levels. This suggests that after 12 hours of F4 treatment, intramembrane lipid transporter transcript levels begin to recover. Sensory histidine kinase activity-related GO terms were downregulated the most after 3 hours of F4 treatment, after which the transcript levels are maintained at those levels for longer treatment periods (Figure 8, Cluster 1). Consistent with these GO terms, the GO

biological processes related to cellular responses to internal and external stimuli (Figure 7C) were enriched, as were the GO Cellular Components associated with the plasma membrane (GO:0005886, GO:0031226, GO:0005887) and cell periphery (GO:0071944) (Figure 7D). These GO terms suggest that Reagent F4 might suppress polarized cell expansion by influencing lipid asymmetry and transport at the plasma membrane. Of all the downregulated DEGs, the genes involved in ATPase-coupled intramembrane lipid transport activity known as plant P4 ATPases/Aminophospholipid ATPases (ALAs) or lipid flippases are particularly interesting. Lipid flippases catalyze the translocation of lipids from the extracellular to the cytosolic side, maintaining transbilayer lipid asymmetry, which plays a role in establishing and maintaining cell polarity (Zhang et al., 2020), tip growth in pollen tubes (Poulsen et al., 2008; Yang et al., 2022a; Zhou et al., 2020), and cell expansion (Davis et al., 2020). In my Reagent F4-treated dataset, P4 ATPase levels steadily declined over time (Figure 9A).

CHAPTER II: IDENTIFICATION OF A NEW CHEMICAL AND ITS MECHANISM OF ACTION THROUGH DARTS-LC-MS/MS

Identification of Reagent F4's mechanism of action through DARTS assay.

To identify the protein target of Reagent F4, I performed a drug affinity responsive target stability (DARTS) assay(Lomenick et al., 2009; Pai et al., 2015), which utilizes the principle of reduced susceptibility of ligand-bound proteins to proteases. To this end, I extracted total protein from 5- days old WT protonema and incubated the lysates with Reagent F4 and DMSO as control, and then digested with different dilutions of Pronase (Fig. 10A). These samples were then analyzed through mass spectrometry. Fold changes were calculated by dividing the intensity values of 100 μM F4 with the intensity values of DMSO (Fig. 10B, Table S3). Out of the proteins enriched > 15-fold, I identified the protein Apolipoprotein-like5 (PpAPL5) for further characterization. PpAPL5 consists of a signal

peptide at the N-terminal, with two coiled-coil domains and a C-terminal transmembrane domain and disordered residues and notably, it contains an apolipoprotein A-I region (Fig. 11A). In mammalian cells, apolipoprotein A-I component of lipoproteins have been shown to induce actin stress fiber formation in cultured endothelial cells (Pellegrino et al., 2004). Additionally, binding of apolipoprotein A-I to the extracellular domains of ABCA1, activates Cdc42 signaling, and thereby actin polymerization, in human fibroblasts (Nofer et al., 2006). To identify PpAPL homologs and orthologs in *Physcomitrium patens* (PpAPL) and other organisms, I queried the *Physcomitrium* genome (Phytozome v.13, v.3.0) using the PpAPL5 amino acid sequence. Four homologs of PpAPL5 were detected. Three putative orthologs of PpAPL5 were detected in *Arabidopsis thaliana*, four orthologs in *Oryza sativa*, five orthologs in *Zea mays* as well as three orthologs in *Sphagnum fallax*, two orthologs in *Ceratopteris richardii* and one ortholog in *Marchantia polymorpha*. All the *P. patens* APL genes closely form a clade with the other bryophytes and pteridophytes. The angiosperm orthologs form a separate clade. Arabidopsis orthologs do not particularly group with any other orthologs and form an outgroup with one of the orthologs. My phylogenetic analysis suggests that the PpAPL genes might be more specifically conserved in mosses (Fig. 11B).

Effect of PpAPL5 overexpression on P. patens morphology and sensitivity to Reagent F4.

To characterize the function and binding of PpAPL5 to Reagent F4, I generated β-estradiol-inducible overexpression lines of PpAPL5 with a C-terminal Citrine fusion tag (Table S4). To assess the impact of PpAPL5 overexpression on colony size, I inoculated 4-day-old PpAPL5 overexpression lines #4 and #21, along with wild-type (WT) protonemata, as small colonies on BCDAT agar media supplemented with 1 μM β-estradiol. After seven days of induction, phenotypic analysis showed no significant effects on the colony size of the *P. patens* protonemata (Fig. 12A, B). Furthermore, I aimed to investigate the sensitivity

of PpAPL5 overexpression to Reagent F4. To do this, I induced 5-day-old protonemata with 1 μM β-estradiol for 16 hours by transferring the cellophane containing the protonemata onto BCDAT agar plates supplemented with β-estradiol. After the 16-hour induction period, the protonemata were transferred to BCDAT agar plates containing 1 μM β-estradiol and the specified compounds. Measurements of subapical cell length revealed that samples treated with 100 μM Reagent F4 (Fig. 12C, D) showed shorter cells, yet the overexpression of PpAPL5 did not appear to elicit either a hypersensitive or hyposensitive response to Reagent F4 as the length of subapical cells of PpAPL5iOx lines after β-estradiol induction, were neither significantly shorter nor longer than the WT samples treated with Reagent F4. The findings suggest that PpAPL5 overexpression does not facilitate the effects of Reagent F4 on the morphology of *P. patens* protonemata.

PpAPL5 localizes to the endoplasmic reticulum and is prone to aggregation.

With the N-terminal signal peptide in the PpAPL5 sequence, I tried to ascertain the localization of PpAPL5. Prediction of subcellular localization with DeepLoc2.0 (https://services.healthtech.dtu.dk/services/DeepLoc-2.0/) revealed a high probability for endoplasmic reticulum localization. This prediction was substantiated by observing the C-terminally Citrine tagged PpAPL5 overexpression lines. Samples were induced with 10 nM β-estradiol for 16 hours and observed using a confocal microscope. PpAPL5 localizes to the endoplasmic reticulum. For control, I observed an ER marker (SP-mCherry-HDEL) and observed a scaffold-like accumulation at the tip of the apical cell in samples treated with DMSO. This accumulation of ER was lost upon 1 hour of 100 μM Reagent F4 treatment. Furthermore, although PpAPL5 localized to the ER, the overexpression lines produced more ER sheet-like structures (Fig. 13). Additionally, treatment with 100 μM Reagent F4 also led to an overaccumulation of aggregates in the PpAPL5iOx-Citrine lines (Fig. 13). When PpAPL5iOx-Citrine was expressed in the background of ER marker (SP-mCherry-

HDEL), it revealed the colocalization of PpAPL5 and ER. This suggests that overexpression of PpAPL5 alters the ER morphology by inducing more ER sheet-like structures (Fig. 14, upper panel). Treatment with Reagent F4 increases PpAPL5 aggregation but does not directly affect ER morphology (Fig. 14, lower panel).

PpAPL5 localizes to the endoplasmic reticulum and is prone to aggregation.

Due to altered ER morphology induced by PpAPL5 overexpression, I wanted to investigate if this change in ER morphology induced by PpAPL5 overexpression has any effects on the actin organization and to that end, I introduced pT1OG-LifeAct-mCherry plasmid in the background of PpAPL5iOx-Citrine background. Upon PpAPL5 overexpression, no change in actin organization was observed (Fig. 15, left panel) as an intact actin foci is observed in samples induced with 10 nM β-estradiol and 0.1% DMSO. Treatment of samples that were induced with 10 nM β-estradiol, with 100 μM Reagent F4 for 1 hour caused actin depolymerization as well as PpAPL5 aggregation (Fig. 15, right panel). This suggests that Reagent F4 might be acting on the actin cytoskeleton and PpAPL5 through different processes and the depolymerization of actin induced by Reagent F4 does not cause PpAPL5 aggregation or vice versa.

PpAPL5 localizes to the endoplasmic reticulum and is prone to aggregation.

To validate the binding ability of Reagent F4 with PpAPL5, I tested the proteolytic degradation of PpAPL5 protein in the absence or presence of 100 μM Reagent F4 (digested with pronase) in protein lysates from 5-day-old protonemata of PpAPL5iOx-Cirine. Total protein lysate from transgenic lines expressing PpAPL5iOx-Citrine was extracted and protein concentration was confirmed with Bradford assay. The lysate was then divided into two aliquots and treated for an hour at room temperature, with 100uM Reagent F4 and

equivalent volume of DMSO, as control. The aliquots were then subjected to proteolytic digestion by adding different dilutions of Pronase to the aliquots (1:300, 1: 100 and no Pronase) for 30 minutes at room temperature. After immunoblotting, the PpAPL5iOx-Cirine, which has a molecular weight of 78kDa (including the Citrine tag), under Reagent F4 treatment was not protected against proteolysis at different dilutions of Pronase. The band near 70kDa (marked with an arrowhead) was lost upon Pronase digestion and much brighter free-GFP was observed. These observations indicate that Pronase is able to cleave PpAPL5 and since GFP is resistant to proteolysis (Bokman and Ward, 1981), it leads to an increased free-GFP signal in the Pronase treated samples. These results collectively indicate that Reagent F4 does not bind with PpAPL5 (Fig. 16) and that this binding is not responsible for the biological effect of Reagent F4 on *P. patens*.

Discussion

Cell polarity refers to the asymmetric organization of cellular components essential for growth and development. Plant cells establish cell polarity for directional tip growth or cell shape determination (e.g., root hairs, pollen tubes or pavement cell) (Hepler et al., 2001; Settleman, 2005). Polarity is driven by the localized distribution of signaling molecules, proteins, lipids, cytoskeletal elements, and vesicle trafficking pathways, enabling plants to adapt to environmental cues and ensure proper organ formation and tissue differentiation. In this study, I established an unbiased chemical screening system using *P. patens* protonemata and demonstrated the role of small molecules in regulating tip growth. I identified Reagent F4, a small molecule that perturbs tip growth by inducing loss of the apical gradient of ROP in protonema apical cells and depolymerization of the actin cytoskeleton, thereby affecting cell expansion, therefore, tip growth of protonemata. Transcriptomic analyses of the effect of Reagent F4 revealed a significant impact on the modulation of genes involved in lipid transport. From these findings, I speculate that Reagent F4 influences tip growth. Reagent F4 induces loss of apical ROP gradient in apical cells and ectopic localization in the lateral membranes of protonemal cells. Although I examined the transcriptomic regulation by F4 on RNA-seq analysis, I did not find any significant changes in the transcript levels of the 4 *P. patens* ROPs (Eklund et al., 2010) and the ROP signaling-related genes like ROPGAP, RENGAP, ROPGDI, RIC (Bascom et al., 2019; Eklund et al., 2010) except ROPGEF2 (Fig 9B) where I observed an upregulation of ROPGEF2 across the time course dataset. ROPGEFs convert ROP from its inactive to active form (GDP-to-GTP) and drive polarized cell expansion by forming clusters with ROP (Ruan et al., 2023). Silencing of ROPGEFs in *P. patens* leads to small plants (Bascom et al., 2019). Further investigations are required to confirm the effect of upregulation of ROPGEF2. ROP has been implicated in angiosperms as being essential for accurate actin organization and assembly (Fu et al., 2002, 2001). In my study, Reagent F4 treatment disrupted actin filament organization. The polar accumulation of ROP relies on its

prenylation motif and interactions with anionic phospholipids at the plasma membrane (Saavedra et al., 2011; Yi and Goshima, 2020). Therefore, it is possible that the mislocalization of ROP, triggered by perturbation of ROP-membrane interactions upon Reagent F4 application, contributed to the loss of polarized actin foci and subsequent actin filament depolymerization.

It is unclear whether Reagent F4 interacts or binds with ROP or actin directly, but studies in yeast have shown that appropriate polarized localization of the yeast ortholog of ROP, Cdc42, is facilitated by transbilayer lipid flipping (Saito et al., 2007). Lipid asymmetry at the plasma membrane, mediated by the lipid flippase complex, enables fast Cdc42 recycling (Das et al., 2012). Plant P4 ATPases, also known as aminophospholipid ATPases (ALAs) or lipid flippases, transport lipids from the extracellular to the cytosolic side of the membrane. *Arabidopsis* contains 12 P4 ATPases, with varying degrees of characterization. ALA3-deficient mutants exhibit mislocalization of polarized PIN1 protein from the basal to the apical membrane in epidermal cells (Zhang et al., 2020) and defective pollen tube growth (Zhou et al., 2020). Loss of ALA3 function also disrupts polar localization of apical phosphatidylserine (PS), indicating its critical role in establishing and maintaining apical PS distribution in pollen tubes. Furthermore, *Arabidopsis* ROP6 has been shown to bind to phosphatidylinositol-3,5-bisphosphate (PtdIns(3,5)P2), phosphatidylinositol-4,5-bisphosphate (PtdIns(4,5)P2) and other anionic phospholipids like PS (Zhou et al., 2020), suggesting that ROP can directly interact with a variety of lipid substrates. These reports, along with my transcriptomics data where lipid flippases-related GO terms were highly enriched in the downregulated DEGs, suggest that lipid asymmetry mediated by flippases in *P. patens* might regulate interaction with small GTPases like ROP and affect its localization by changing the lipid distribution throughout the bilayer. Defective lipid asymmetry also leads to inefficient recruitment of pollen-specific receptor kinases in Arabidopsis pollen tubes (Yang et al., 2022b), which activate ROPGEF in pollen tubes, leading to ROP activation. Additionally, lipid asymmetry is required for the

626 activation of the Arp2/3 complex that promotes actin filament assembly (Bezanilla et al.,
627 2015; Saarikangas et al., 2010). Identifying the lipid environment of the plasma membrane
628 under the influence of Reagent F4 could provide deeper insights into the substrate
629 specificity of *P. patens* ROP. This may also reveal upstream factors involved in ROP
630 recruitment to the membrane, ultimately regulating polarized tip growth in *P. patens*.

631 Target identification through DARTS did not yield positive results with Reagent F4
632 not having a protective effect on PpAPL5 from proteolytic degradation. However, PpAPL5
633 was observed to influence the ER morphology by inducing ER sheet-like structures. This
634 suggests that PpAPL5 could be an ER-resident protein involved in ER remodeling in *P.*
635 *patens.*

636 Several reports have utilized small molecules to investigate plant development
637 (Drakakaki et al., 2011; Kimata et al., 2023; Sakai et al., 2017) and I report a novel
638 chemical, Reagent F4, that affects polarized cell expansion by causing defects in cell
639 elongation, actin polymerization, and proper ROP localization maintenance in *P. patens*.
640 Identification of Reagent F4 target proteins provides valuable knowledge in clarifying the
641 mechanisms involved in tip growth and polarized cell expansion in *P. patens* and in plants,
642 in general, as ROP and actin-based tip growth regulation appear to be well conserved (Orr
643 et al., 2020).

644

Figures

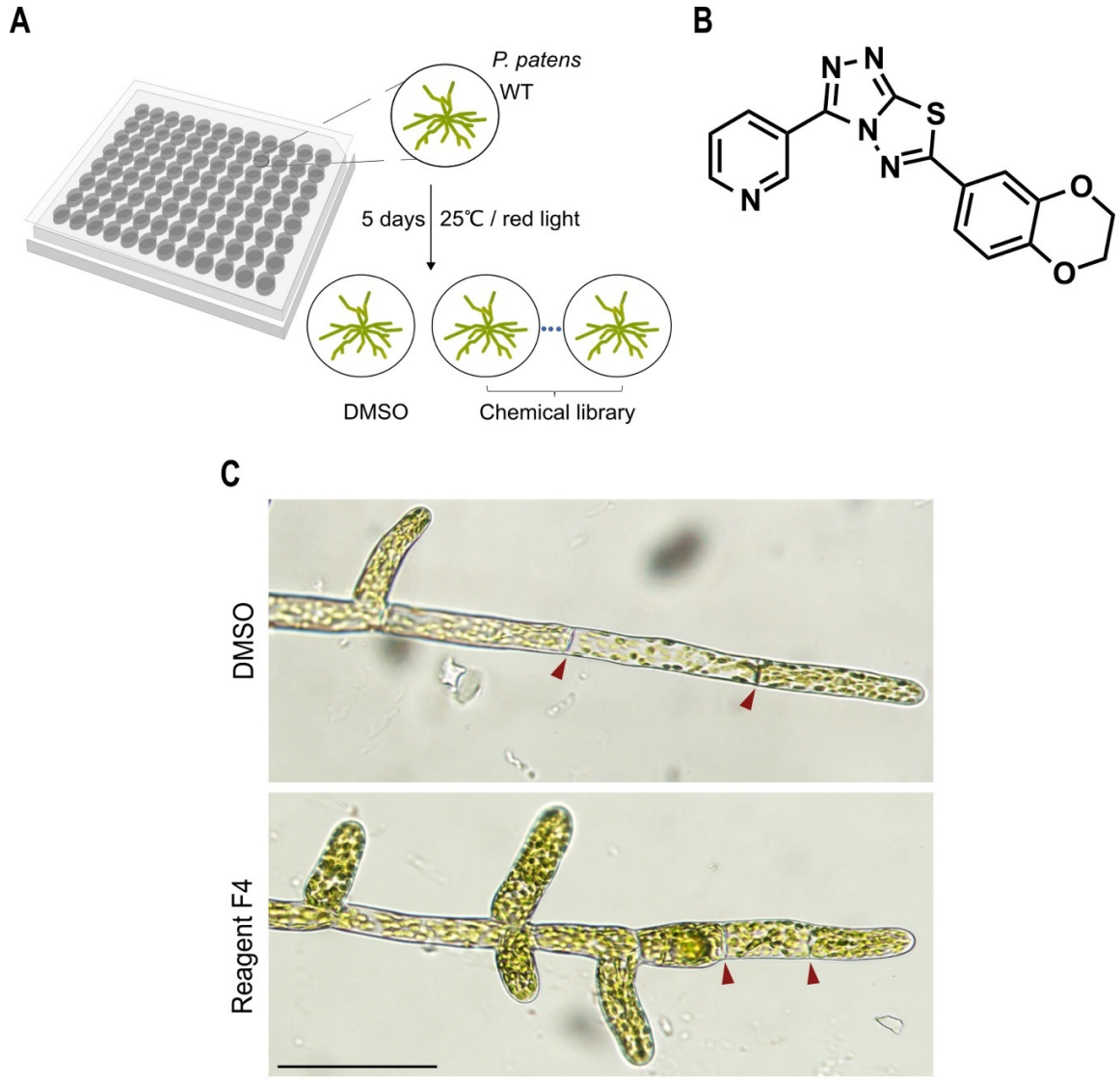

FIGURE 1

Figure 1. Chemical screening for compounds that affect tip growth.

A. Schematic representation of the phenotype-based screen using wild-type (WT) *P.*

649 *patens* protonemata. Samples were first incubated under red light for five days to
650 suppress side branch formation and then treated with the chemical library,
651 followed by incubation under white light for two days.

652 B. Chemical structure of Reagent F4.

653 C. Brightfield images of WT protonema treated with 0.1% DMSO as a control and
654 10 μM Reagent F4 after one day of treatment. Red arrowheads indicate septum.
655 Scale bar, 100 μm.
656

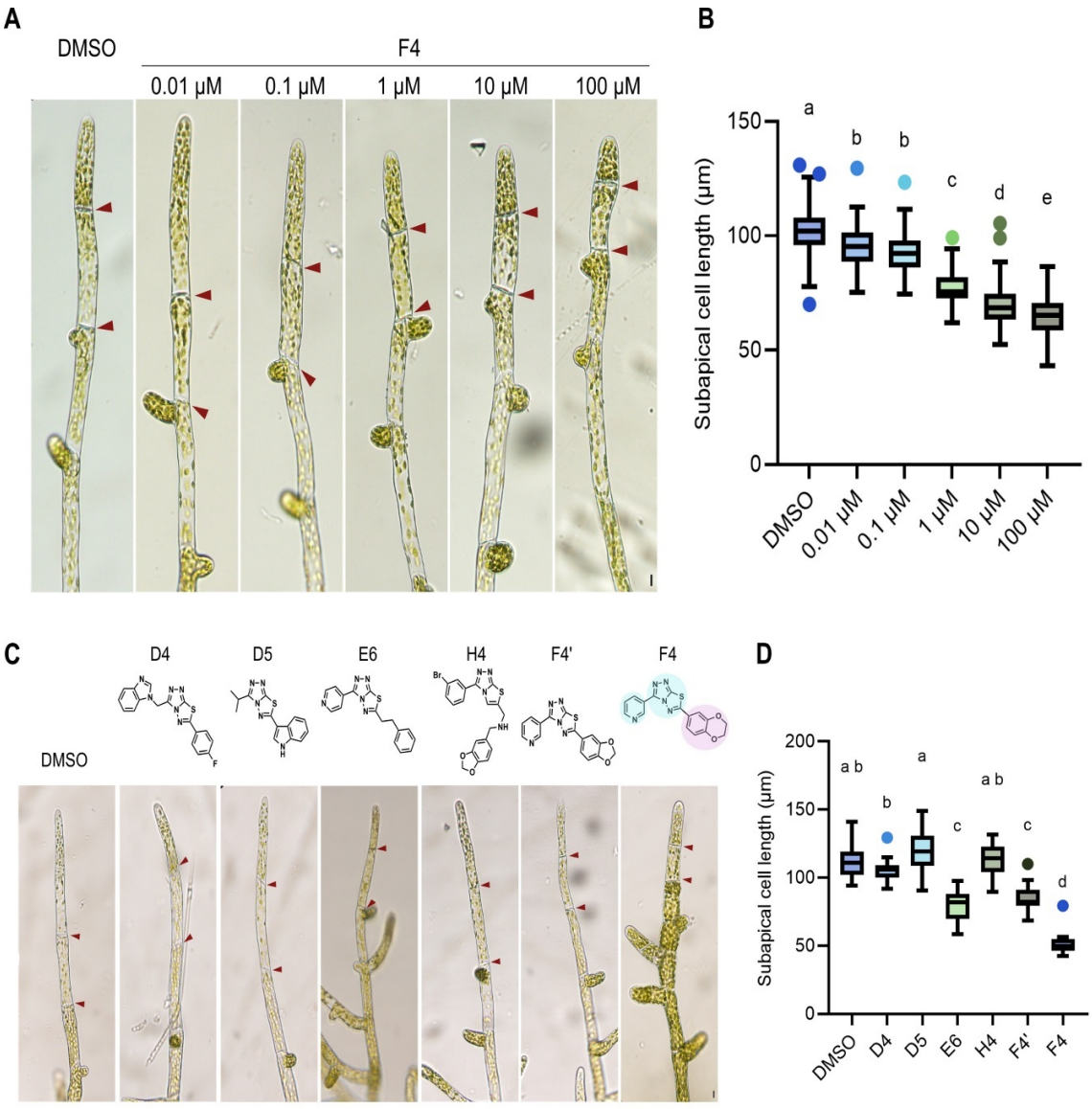

FIGURE 2

Figure 2. Reagent F4 affects cell elongation in a dose-dependent manner.

A. Brightfield images of WT protonema treated with 0.1% DMSO as control and different concentrations of Reagent F4, after one day of treatment. Red arrowheads

indicate septum. Scale bar, 10 μm.

B. Quantification of subapical cell length after treatment with 0.1% DMSO and different concentrations of Reagent F4, after one day of treatment (n = 130, 119, 109, 98, 115, 105). Different letters indicate statistically significant differences (one-way ANOVA and Tukey's multiple comparison test $p < 0.01$).

C. Chemical structures of Reagent F4 analogs with corresponding brightfield images of WT protonema treated with 100 μM of each compound. Red arrowheads indicate septum. Scale bar, 10 μm.

D. Quantification of subapical cell length after treatment with 0.1% DMSO and different analogs of Reagent F4, after two days of treatment (n = 14, 19, 15, 10, 17, 17, 11). Different letters indicate statistically significant differences (one-way ANOVA and Tukey's multiple comparison test $p < 0.01$).

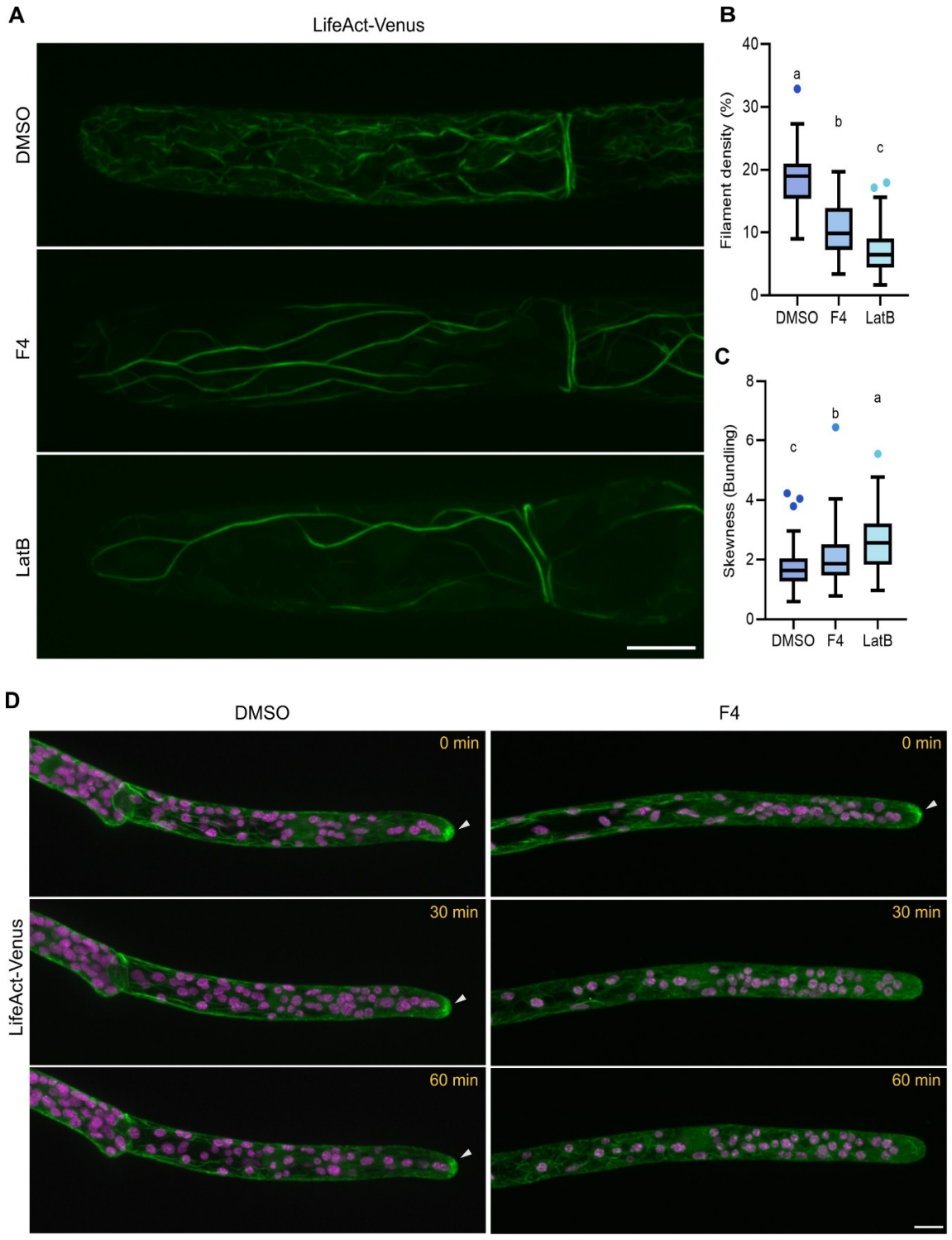
A
LifeAct-Venus
DMSO
F4
LatB
B
Filament density (%)
40
30
20
10
0
a
b
c
DMSO
F4
LatB
C
Skewness (Bundling)
8
6
4
2
0
c
b
a
DMSO
F4
LatB
D
DMSO
F4
LifeAct-Venus
0 min
30 min
60 min
0 min
30 min
60 min

FIGURE 3

Figure 3. Reagent F4 induces actin depolymerization and loss of actin foci.

A. Confocal images of 6-day LifeAct-Venus transgenic protonema grown in BCD media in glass bottom dishes, treated with 0.1% DMSO as control, 100 µM Reagent F4, and 1 µM Latrunculin B, after 2 hours of treatment. Scale bar, 10 µm.

B. Quantification of filament density (denoted in percentage) of actin filaments in LifeAct-Venus transgenic protonema, treated with 0.1% DMSO (n = 88) as control, 100 µM Reagent F4 (n = 88) and 1 µM Latrunculin B (n = 101), after 2 hours of treatment. Different letters indicate statistically significant differences (one-way ANOVA and Tukey's multiple comparison test $p < 0.01$).

C. Quantification of skewness of fluorescence intensity denoting bundling of actin filaments in LifeAct-Venus transgenic protonema, treated with 0.1% DMSO (n = 88) as control, 100 µM Reagent F4 (n = 88) and 1 µM Latrunculin B (n = 101), after 2 hours of treatment. Different letters indicate statistically significant differences (one-way ANOVA and Tukey's multiple comparison test $p < 0.05$).

D. Confocal images of 6-day LifeAct-Venus transgenic protonema grown in BCD media in glass bottom dishes, treated with 0.1% DMSO (n = 16) as control and 100 µM Reagent F4 (n = 19). Timepoint 0 minutes denotes before treatment with the indicated compounds. The green channel represents LifeAct-Venus, and the magenta channel represents chlorophyll. White arrowheads indicate actin foci. Scale bar, 10 µm.

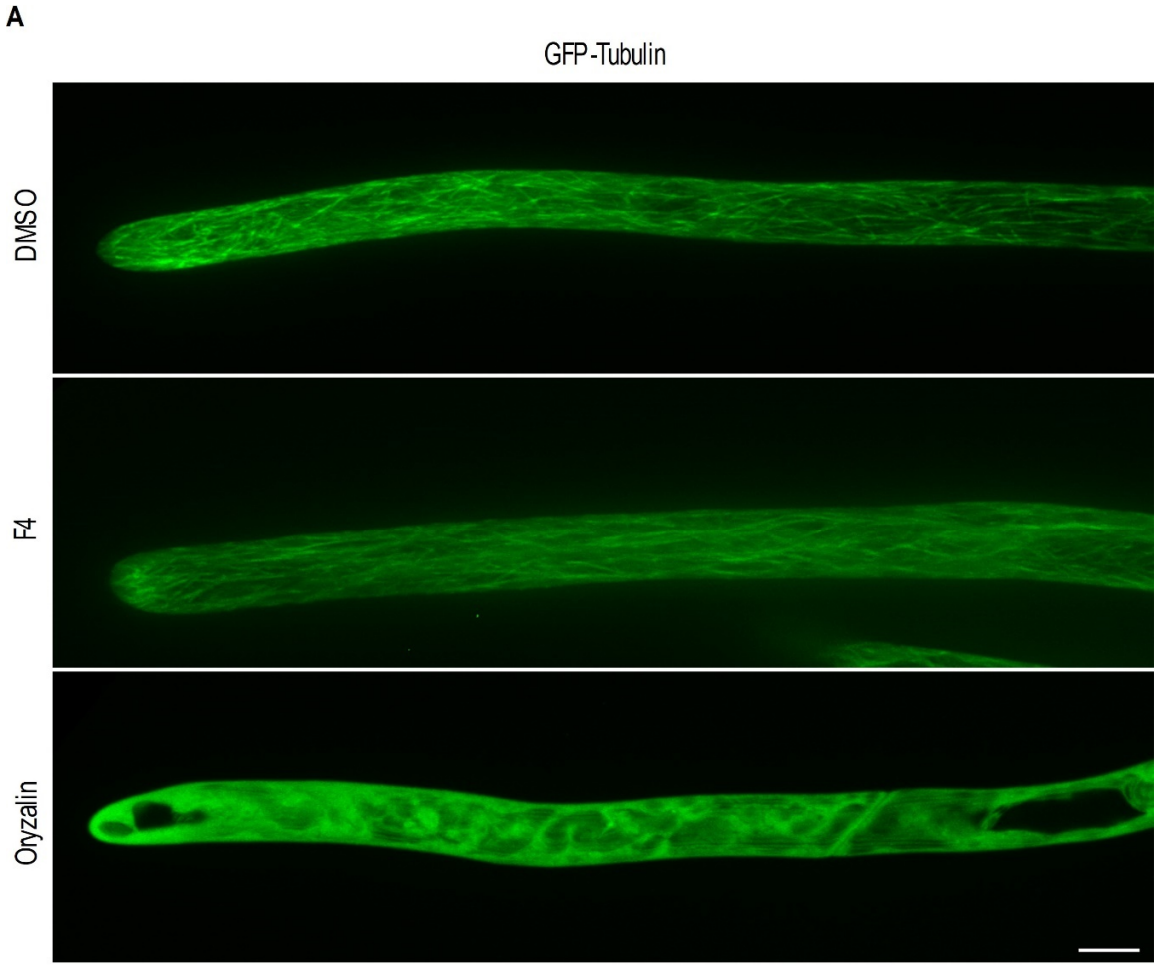

FIGURE 4

Figure 4. Reagent F4 does not affect microtubule organization post-acute treatment in P. patens.

A. Confocal images of 6-day GFP-Tubulin transgenic protonema grown in BCD media in glass bottom dishes, treated with 0.1% DMSO as control (n = 20), 100 µM Reagent F4 (n = 22) and 10 µM Oryzalin (n = 13), after 2 hours of treatment. Scale bar, 10 µm.

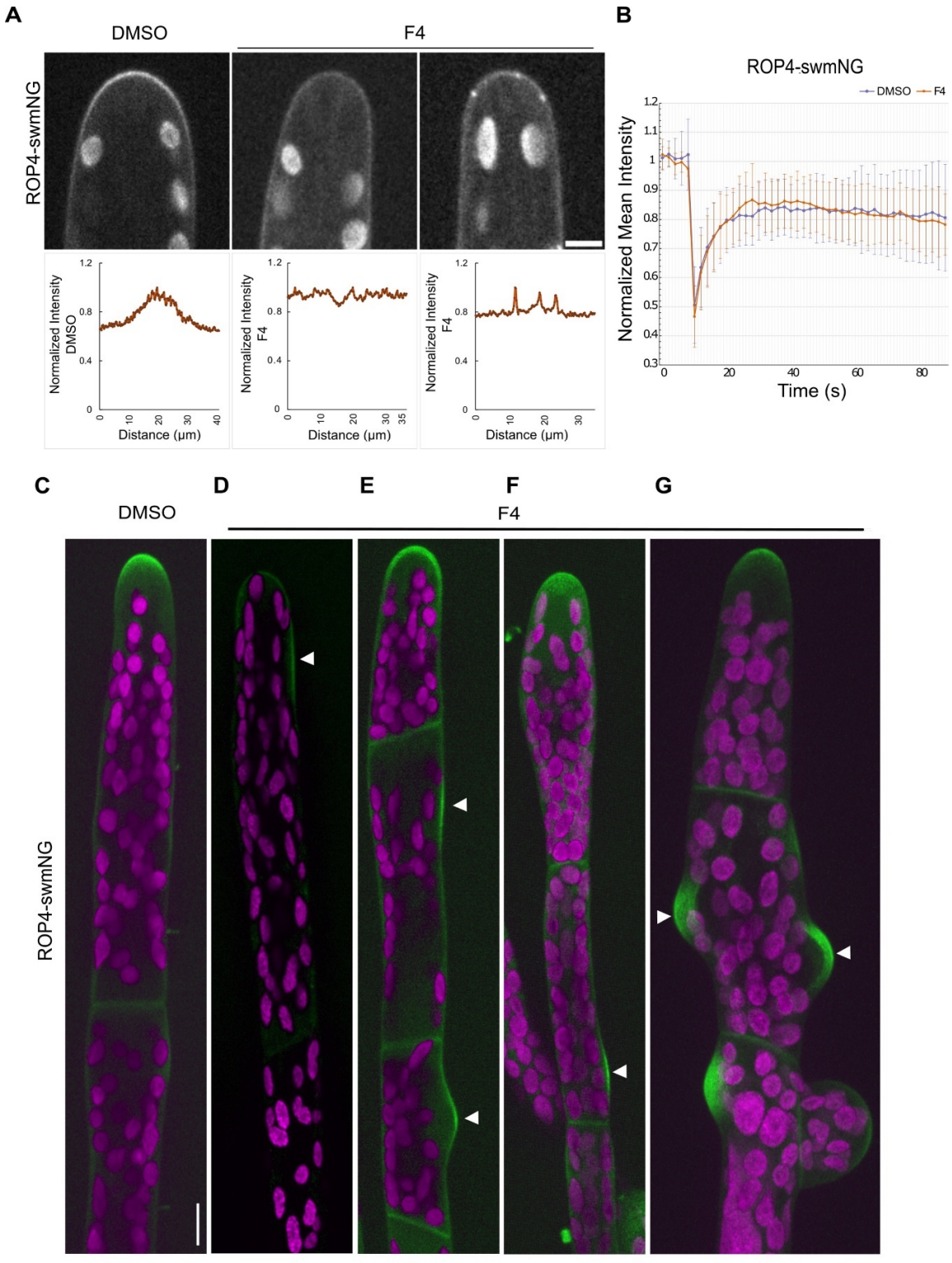
A
DMSO
F4
ROP4-swmNG
Normalized Intensity DMSO
Normalized Intensity F4
Normalized Intensity F4
Distance (μm)
Distance (μm)
Distance (μm)
B
ROP4-swmNG
DMSO
F4
Normalized Mean Intensity
Time (s)
C
D
E
F
G
DMSO
F4
ROP4-swmNG

FIGURE 5

Figure 5. Acute treatment with Reagent F4 causes loss of apical ROP gradient in apical cells.

A. Example confocal images of 6-day old ROP4-swmNG transgenic protonema grown in BCDATG media in glass bottom dishes, treated with 0.1% DMSO (n = 24) as control and 100 µM Reagent F4 (n = 40), after 30 minutes of treatment and signal intensity quantification of protonemal apical cell after treatment with the indicated compounds. Two different kinds of phenotypes were observed in samples treated with Reagent F4 consisting of total loss of the apical ROP gradient as well as aggregation of ROP at certain regions. Graphs were generated by measuring the signal intensity along a manually drawn line tracing the plasma membrane of the cell. Scale bar, 5 µm.
B. FRAP analysis of ROP4-swmNG, treated with 0.1% DMSO (n = 16) as control and 100 µM Reagent F4 (n = 19), after 30 minutes of treatment. The normalized mean fluorescence intensity of ROP4-swmNG was measured in the photobleached region of interest (ROI) and plotted over time. Each line is the average normalized intensity of all cells with the indicated treatment. Error bars represent standard deviation.
C. Long-term exposure to Reagent F4 reveals aberrant ROP localization in *P. patens.* Confocal images of 7-days-old ROP4-swmNG transgenic protonema grown in BCDATG media in glass bottom dishes, treated with 0.1% DMSO as control, observed after 24 hours of treatment. Scale bar, 10 µm.
D. Long-term exposure to Reagent F4 reveals aberrant ROP localization in P. *patens.* Confocal images of 7-days-old ROP4-swmNG transgenic protonema grown in BCDATG media in glass bottom dishes, treated with 100 µM Reagent F4, observed after 24 hours of treatment. White arrowhead indicates ectopic ROP localization on the lateral side of the apical cell. Scale bar, 10 µm.

E. Long-term exposure to Reagent F4 reveals aberrant ROP localization in P. *patens.* Confocal images of 7-days-old ROP4-swmNG transgenic protonema grown in BCDATG media in glass bottom dishes, treated with 100 µM Reagent F4, observed after 24 hours of treatment. White arrowhead indicates ectopic ROP localization in the medial portion of the subapical cell. Scale bar, 10 µm.

F. Long-term exposure to Reagent F4 reveals aberrant ROP localization in P. *patens.* Confocal images of 7-days-old ROP4-swmNG transgenic protonema grown in BCDATG media in glass bottom dishes, treated with 100 µM Reagent F4, observed after 24 hours of treatment. White arrowhead indicates ectopic ROP localization at the basal end of the subapical cell. Scale bar, 10 µm.

G. Long-term exposure to Reagent F4 reveals aberrant ROP localization in P. *patens.* Confocal images of 7-days-old ROP4-swmNG transgenic protonema grown in BCDATG media in glass bottom dishes, treated with 100 µM Reagent F4, observed after 24 hours of treatment. White arrowheads indicate ectopic side branch protrusions with normal ROP localization at the tip of the protrusions. Scale bar, 10 µm.

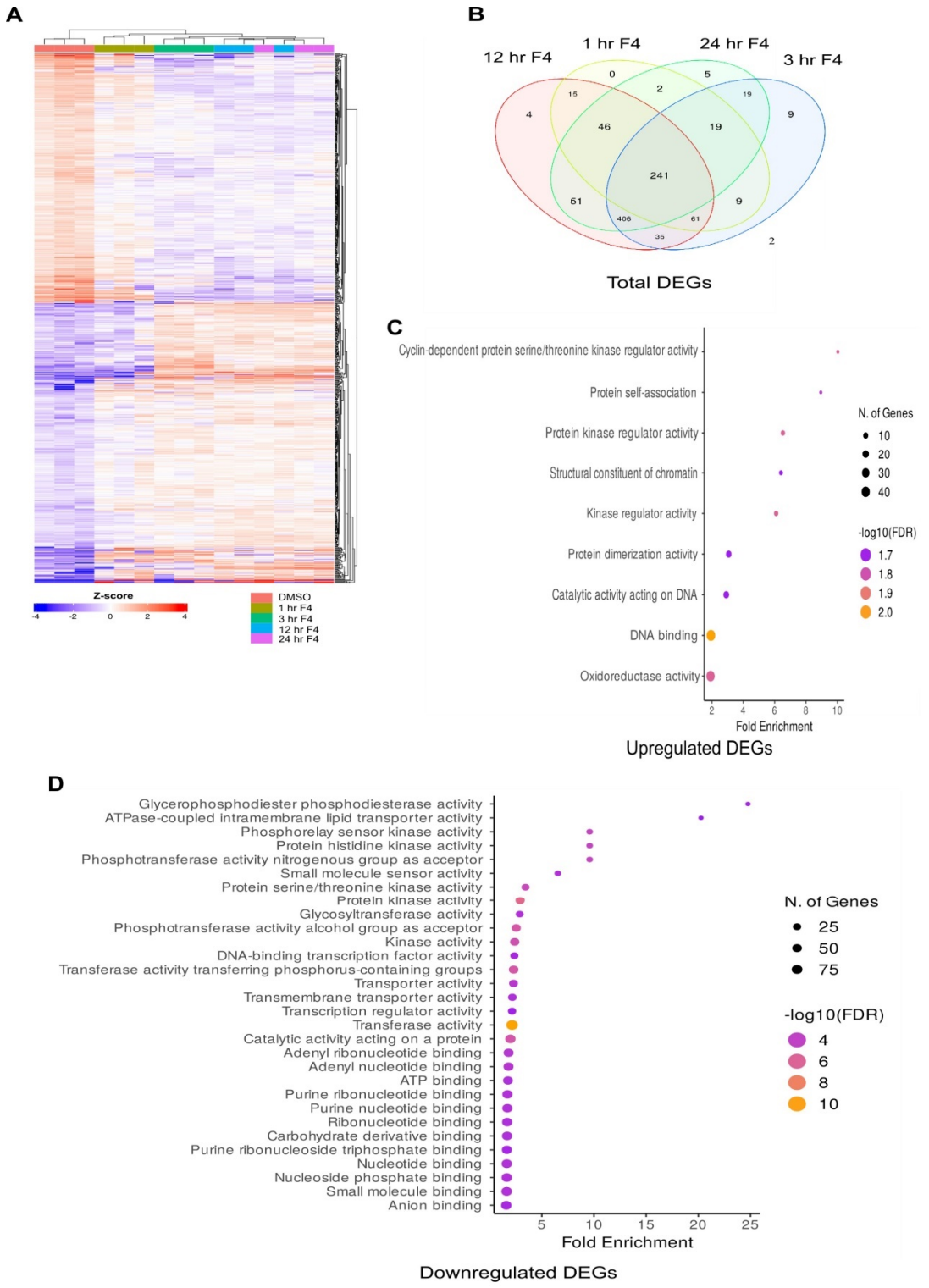
A
Z-score
-4
-2
0
2
4
DMSO
1 hr F4
3 hr F4
12 hr F4
24 hr F4
B
12 hr F4
1 hr F4
24 hr F4
3 hr F4
0
5
15
2
19
4
9
46
19
241
51
9
406
61
35
2
Total DEGs
C
Cyclin-dependent protein serine/threonine kinase regulator activity
Protein self-association
Protein kinase regulator activity
Structural constituent of chromatin
Kinase regulator activity
Protein dimerization activity
Catalytic activity acting on DNA
DNA binding
Oxidoreductase activity
2
4
6
8
10
Fold Enrichment
N. of Genes
10
20
30
40
-log10(FDR)
1.7
1.8
1.9
2.0
Upregulated DEGs
D
Glycerophosphodiester phosphodiesterase activity
ATPase-coupled intramembrane lipid transporter activity
Phosphorelay sensor kinase activity
Protein histidine kinase activity
Phosphotransferase activity nitrogenous group as acceptor
Small molecule sensor activity
Protein serine/threonine kinase activity
Protein kinase activity
Glycosyltransferase activity
Phosphotransferase activity alcohol group as acceptor
Kinase activity
DNA-binding transcription factor activity
Transferase activity transferring phosphorus-containing groups
Transporter activity
Transmembrane transporter activity
Transcription regulator activity
Transferase activity
Catalytic activity acting on a protein
Adenyl ribonucleotide binding
Adenyl nucleotide binding
ATP binding
Purine ribonucleotide binding
Purine nucleotide binding
Ribonucleotide binding
Carbohydrate derivative binding
Purine ribonucleoside triphosphate binding
Nucleotide binding
Nucleoside phosphate binding
Small molecule binding
Anion binding
5
10
15
20
25
Fold Enrichment
N. of Genes
25
50
75
-log10(FDR)
4
6
8
10
Downregulated DEGs

FIGURE 6

Figure 6. Transcriptional changes in response to short-term and long-term Reagent F4 treatment.

A. Hierarchical clustering of normalized counts of the most differentially expressed genes (DEGs) of Reagent F4 treated samples at different time points, compared to 0.1% DMSO as mock. Clustering of samples was done, along with centering of the genes. Max Z-score = 4.

B. Venn diagram of the total differentially expressed genes, across different treatments and time points.

C. A dot plot that depicts enriched GO terms: Molecular Functions of the upregulated DEGs across all time points. The GO terms were sorted by fold enrichment. The size of the dots denotes the number of genes, and the color corresponds to the log10 (FDR) value, where orange is the high value and purple is the low value.

D. A dot plot that depicts enriched GO terms: Molecular Functions of the downregulated DEGs across all time points. The GO terms were sorted by fold enrichment. The size of the dots denotes the number of genes, and the color corresponds to the log10 (FDR) value, where orange is the high value and purple is the low value.

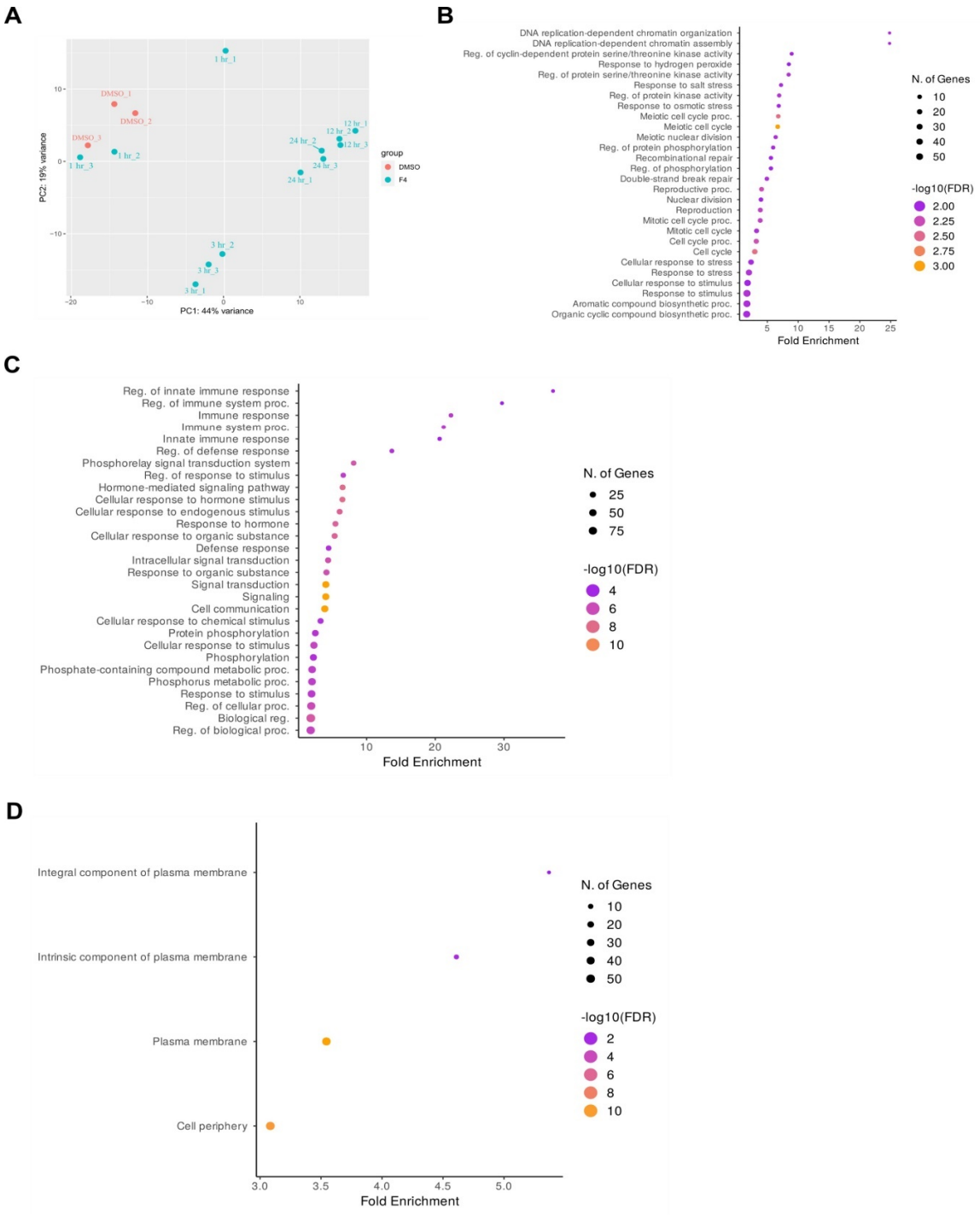
A
1 hr_1
DMSO_1
DMSO_2
DMSO_3
1 hr_2
1 hr_3
12 hr_1
12 hr_2
12 hr_3
24 hr_2
24 hr_3
24 hr_1
3 hr_2
3 hr_3
3 hr_1
PC2: 19% variance
PC1: 44% variance
group
DMSO
F4
B
DNA replication-dependent chromatin organization
DNA replication-dependent chromatin assembly
Reg. of cyclin-dependent protein serine/threonine kinase activity
Response to hydrogen peroxide
Reg. of protein serine/threonine kinase activity
Response to salt stress
Reg. of protein kinase activity
Response to osmotic stress
Meiotic cell cycle proc.
Meiotic cell cycle
Meiotic nuclear division
Reg. of protein phosphorylation
Recombinational repair
Reg. of phosphorylation
Double-strand break repair
Reproductive proc.
Nuclear division
Reproduction
Mitotic cell cycle proc.
Mitotic cell cycle
Cell cycle proc.
Cell cycle
Cellular response to stress
Response to stress
Cellular response to stimulus
Response to stimulus
Aromatic compound biosynthetic proc.
Organic cyclic compound biosynthetic proc.
Fold Enrichment
N. of Genes
10
20
30
40
50
-log10(FDR)
2.00
2.25
2.50
2.75
3.00
C
Reg. of innate immune response
Reg. of immune system proc.
Immune response
Immune system proc.
Innate immune response
Reg. of defense response
Phosphorelay signal transduction system
Reg. of response to stimulus
Hormone-mediated signaling pathway
Cellular response to hormone stimulus
Cellular response to endogenous stimulus
Response to hormone
Cellular response to organic substance
Defense response
Intracellular signal transduction
Response to organic substance
Signal transduction
Signaling
Cell communication
Cellular response to chemical stimulus
Protein phosphorylation
Cellular response to stimulus
Phosphorylation
Phosphate-containing compound metabolic proc.
Phosphorus metabolic proc.
Response to stimulus
Reg. of cellular proc.
Biological reg.
Reg. of biological proc.
Fold Enrichment
N. of Genes
25
50
75
-log10(FDR)
4
6
8
10
D
Integral component of plasma membrane
Intrinsic component of plasma membrane
Plasma membrane
Cell periphery
Fold Enrichment
N. of Genes
10
20
30
40
50
-log10(FDR)
2
4
6
8
10

FIGURE 7

Figure 7. Bulk RNA-seq of short-term and long-term Reagent F4 treated P. patens.

A. Principal component analysis of all the replicates of samples at different time points.

B. A dot plot that depicts enriched GO terms: Biological Processes of the upregulated DEGs across all time points. The GO terms were sorted by fold enrichment. The size of the dots denotes the number of genes, and the color corresponds to the log10 (FDR) value, where orange is the high value and purple is the low value.

C. A dot plot that depicts enriched GO terms: Biological Processes of the downregulated DEGs across all time points. The GO terms were sorted by fold enrichment. The size of the dots denotes the number of genes, and the color corresponds to the log10 (FDR) value, where orange is the high value and purple is the low value.

D. A dot plot that depicts enriched GO terms: Cellular Components of the downregulated DEGs across all time points. The GO terms were sorted by fold enrichment. The size of the dots denotes the number of genes, and the color corresponds to the log10 (FDR) value, where orange is the high value and purple is the low value.

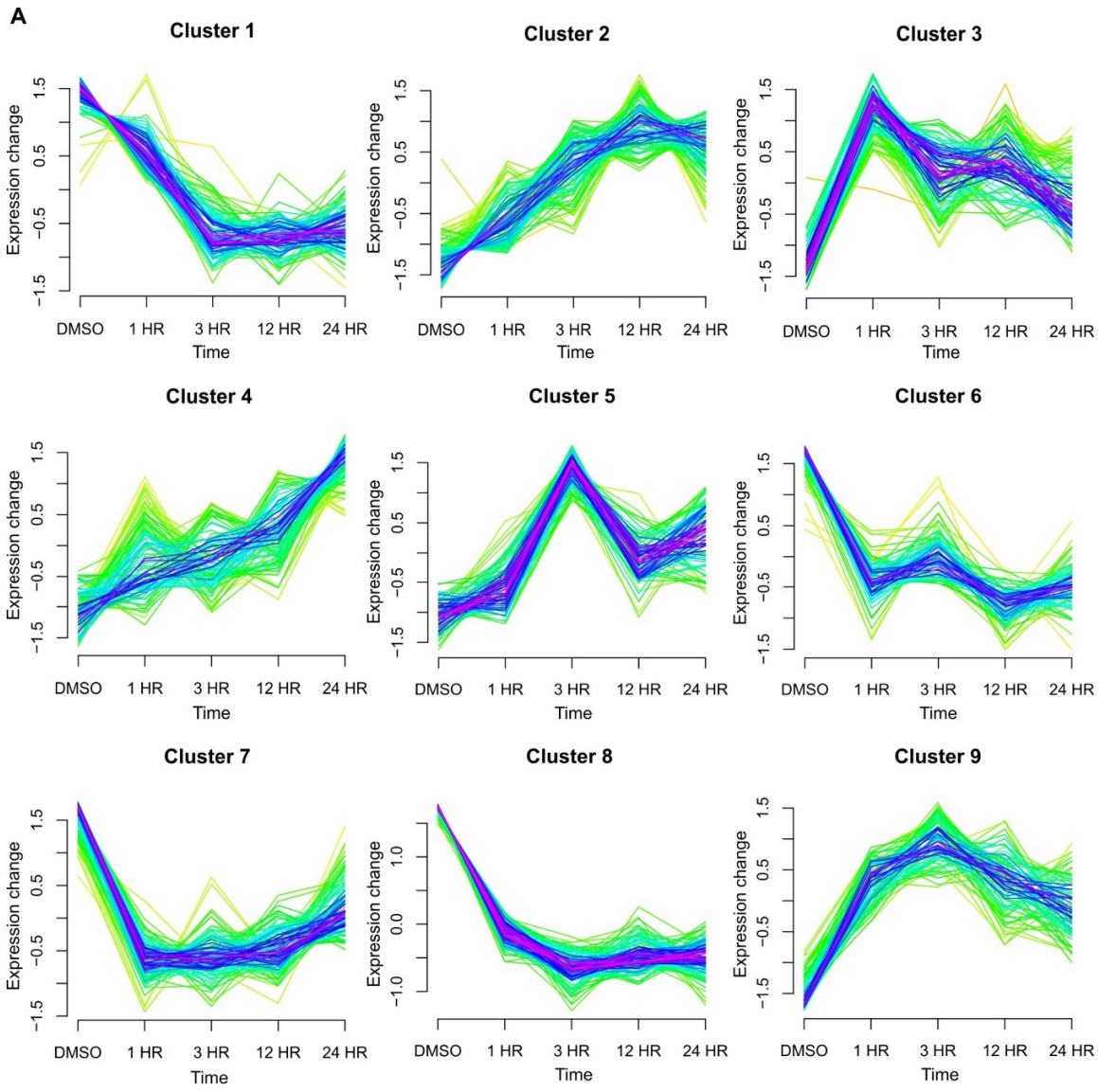

FIGURE 8

Figure 8. Mfuzz clustering of transcripts differentially expresses genes at different time points upon Reagent F4 treatment.

A. Gene profiles of co-expression clusters identified by the Mfuzz clustering program

of DEGs upon Reagent F4 treatment at different time points. The treatment time points are represented on the x-axis (in hours), and the y-axis represents the normalized gene expression value.

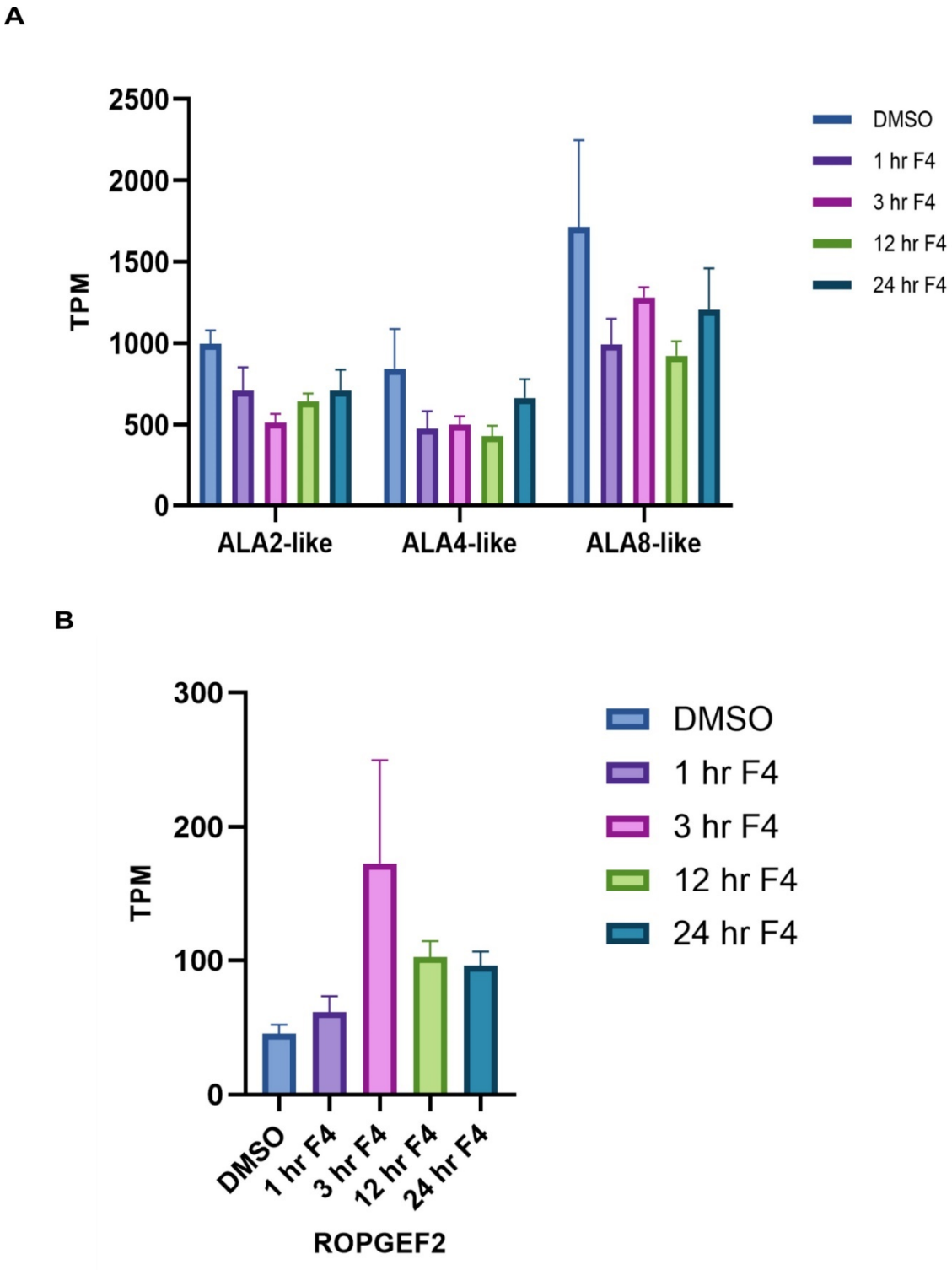
A
2500
2000
1500
1000
500
0
TPM
ALA2-like
ALA4-like
ALA8-like
DMSO
1 hr F4
3 hr F4
12 hr F4
24 hr F4
B
300
200
100
0
TPM
DMSO
1 hr F4
3 hr F4
12 hr F4
24 hr F4
ROPGEF2

FIGURE 9

793

Figure 9. Expression level changes of genes-of-interest upon Reagent F4 treatment.

A. Gene expression profiles of the downregulated lipid flippases in *P. patens* in Reagent F4 treated samples at different time points. The x-axis represents the time points, and the y-axis represents the normalized TPM values with standard deviation (SD) error bars.

B. Gene expression profiles of the upregulated ROPGEF2 in *P. patens* in Reagent F4 treated samples at different time points. The x-axis represents the time points, and the y-axis represents the normalized TPM values with standard deviation (SD) error bars.

A

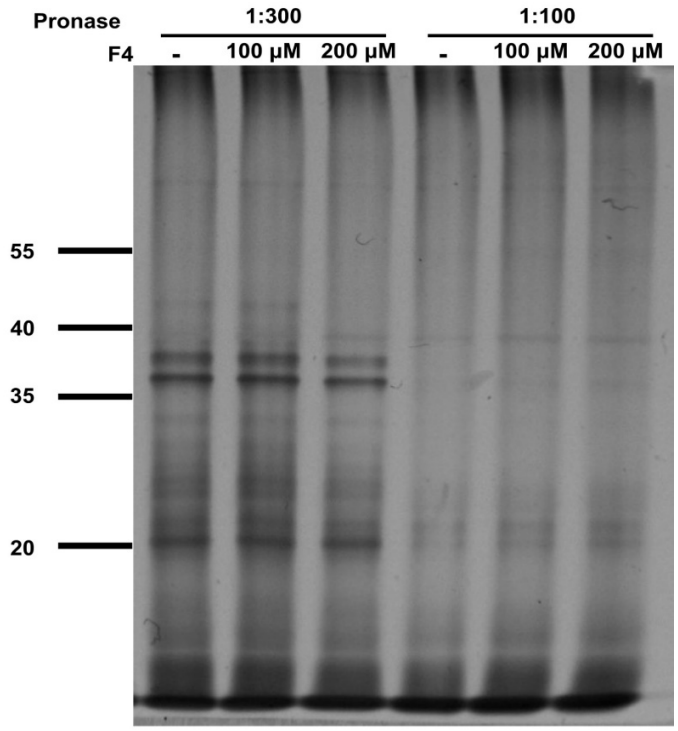

B

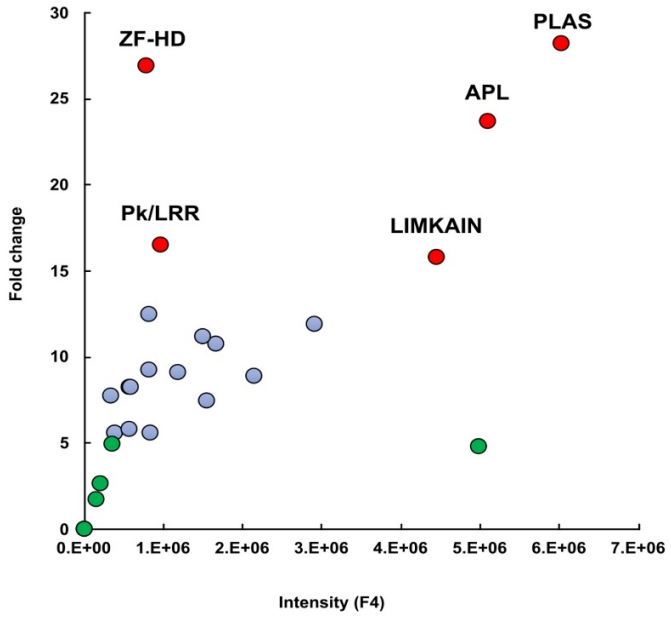

FIGURE 10

804

Figure 10. DARTS using whole cell lysate and enrichment of protected peptides.

A. Whole cell protonemal lysate was treated with DMSO, 100 μM, and 200 μM Reagent F4, and lysates were subjected to Pronase digestion. Silver-stained polyacrylamide gel.

B. Enrichment of peptides in the 100 μM Reagent F4 sample treated with 1:100 Pronase from A revealed by mass spectrometry analysis. Red, protein enriched > 15-fold; green, protein enriched < 5-fold; blue, enriched ≥ 5-fold and/or ≤ 15-fold. ZF-HD: ZF-Homeodomain-like protein; PLAS: Plastocyanin; APL: Apolipoprotein-like protein; Pk/LRR: Leucine-rich repeat protein kinase; LIMKAIN: LIMKAIN B LKAP.

A

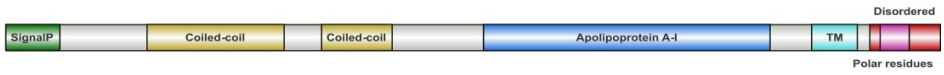
PpApolipoprotein-like5 (PpAPL5)
Disordered
SignalP
Coiled-coil
Coiled-coil
Apolipoprotein A-I
TM
Polar residues

B

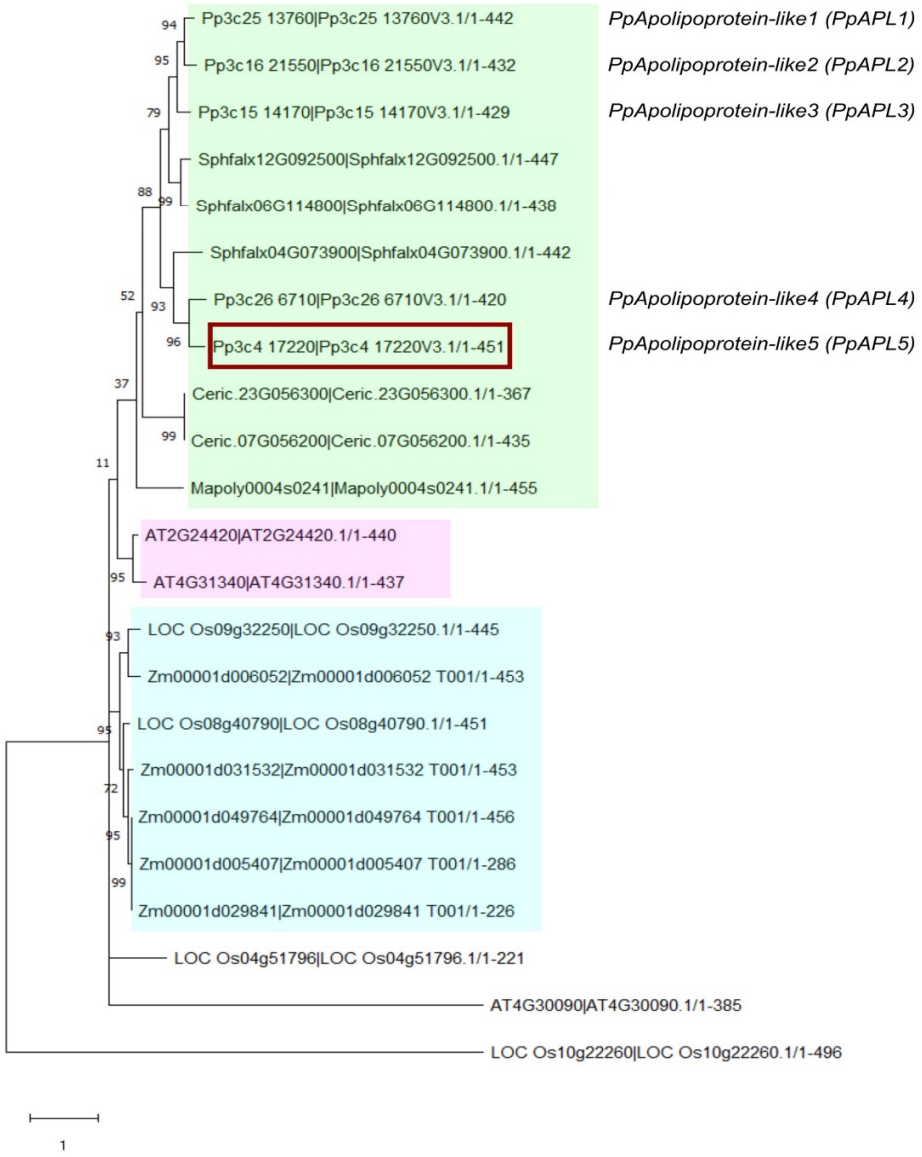
Pp3c25 13760|Pp3c25 13760V3.1/1-442
Pp3c16 21550|Pp3c16 21550V3.1/1-432
Pp3c15 14170|Pp3c15 14170V3.1/1-429
Sphfalx12G092500|Sphfalx12G092500.1/1-447
Sphfalx06G114800|Sphfalx06G114800.1/1-438
Sphfalx04G073900|Sphfalx04G073900.1/1-442
Pp3c26 6710|Pp3c26 6710V3.1/1-420
Pp3c4 17220|Pp3c4 17220V3.1/1-451
Ceric.23G056300|Ceric.23G056300.1/1-367
Ceric.07G056200|Ceric.07G056200.1/1-435
Mapoly0004s0241|Mapoly0004s0241.1/1-455
AT2G24420|AT2G24420.1/1-440
AT4G31340|AT4G31340.1/1-437
LOC Os09g32250|LOC Os09g32250.1/1-445
Zm00001d006052|Zm00001d006052 T001/1-453
LOC Os08g40790|LOC Os08g40790.1/1-451
Zm00001d031532|Zm00001d031532 T001/1-453
Zm00001d049764|Zm00001d049764 T001/1-456
Zm00001d005407|Zm00001d005407 T001/1-286
Zm00001d029841|Zm00001d029841 T001/1-226
LOC Os04g51796|LOC Os04g51796.1/1-221
AT4G30090|AT4G30090.1/1-385
LOC Os10g22260|LOC Os10g22260.1/1-496
PpApolipoprotein-like1 (PpAPL1)
PpApolipoprotein-like2 (PpAPL2)
PpApolipoprotein-like3 (PpAPL3)
PpApolipoprotein-like4 (PpAPL4)
PpApolipoprotein-like5 (PpAPL5)
94
95
79
88
99
52
93
96
37
99
11
95
93
95
72
95
99
1

FIGURE 11

Figure 11. P. patens possesses five Apolipoprotein-like genes.

A. Schematic representations of the PpAPL5 protein domains.
B. An unrooted maximum-likelihood phylogenetic tree with APL amino acid sequences from bryophytes, pteridophytes and angiosperms. *P. patens* APL genes clade with other bryophytes and pteridophytes (green box), angiosperms other than *Arabidopsis* also clade together (blue box). Arabidopsis APL genes group together (red box) with an outlier. Species names are summarised as follows: *Physcomitrium patens* (Pp), *Sphagnum fallax* (Sphfalx), *Ceratopteris richardii* (Ceric), *Marchantia polymorpha* (Mapoly), *Arabidopsis thaliana* (At), *Oryza sativa* (Os) and *Zea mays* (Zm). Numbers on the nodes indicate bootstrap values. PpAPL5 (marked with a red box) was used for further experiments.

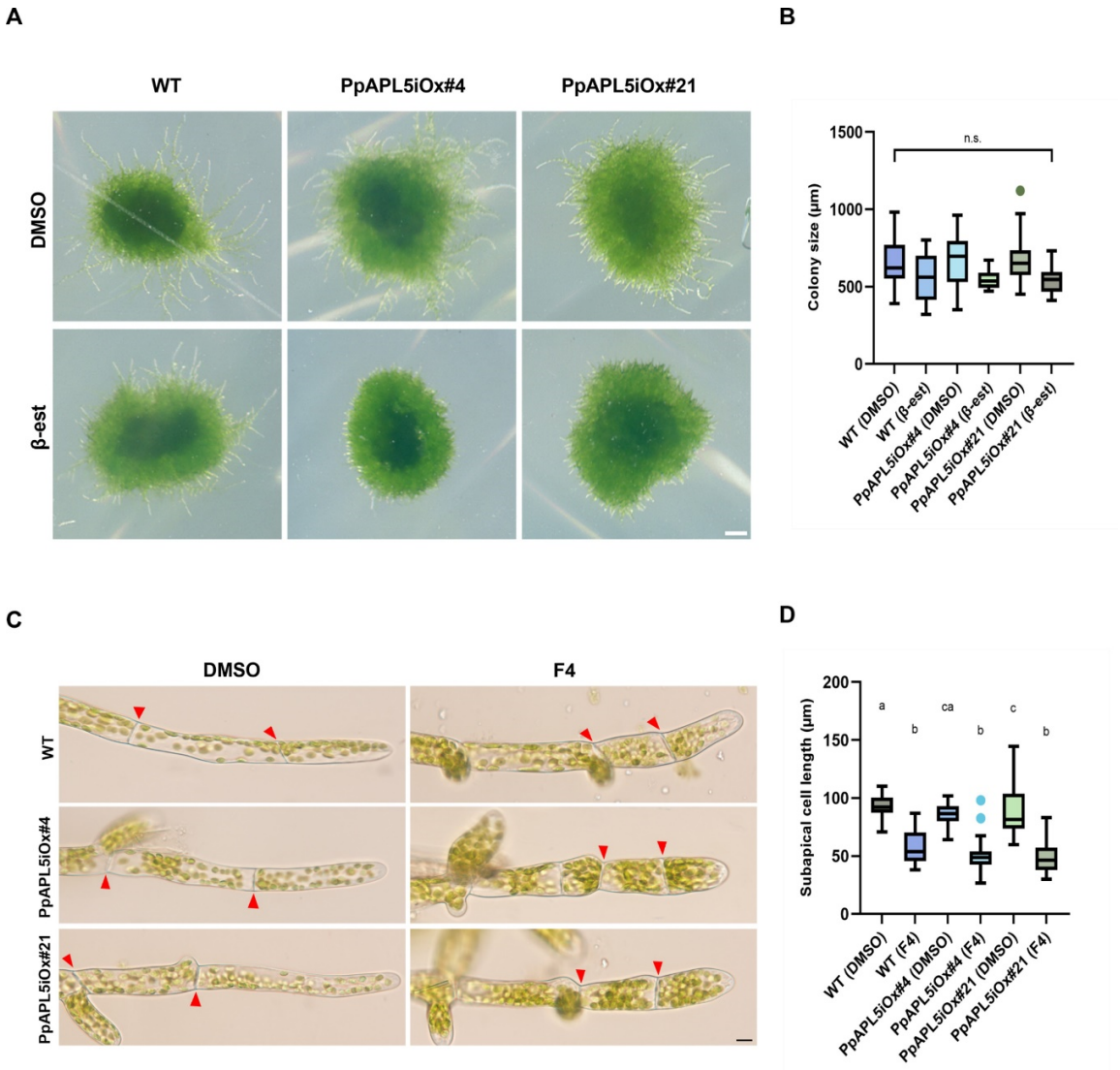

FIGURE 12

Figure 12. Effects of PpAPL5 overexpression on P. patens morphology.

A. Colony growth in wild-type (WT) and PpAPL5iOx lines. Colonies were inoculated onto BCDAT agar plates containing 0.1% DMSO and 1 µM β-estradiol and observed after 7 days. Scale bar, 500 µm.

B. Box-and-whisker plots of normalized colony sizes. Boxes show the interquartile range. N.s. indicates no statistically significant differences (ANOVA and Tukey's post hoc test) (n = 20).

C. Subapical cell length in wild-type (WT) and PpAPL5iOx lines. Samples were induced with 1 μM β-estradiol for 16 hours and then treated with 0.1% DMSO and 100 μM Reagent F4 for one day. Red arrowheads indicate septum. Scale bar, 10 μm.

D. Box-and-whisker plots of normalized colony sizes. Boxes show the interquartile range. Different letters indicate statistically significant differences (ANOVA and Tukey's post hoc test $p < 0.01$) (n = 29,29,25,35,20,38).

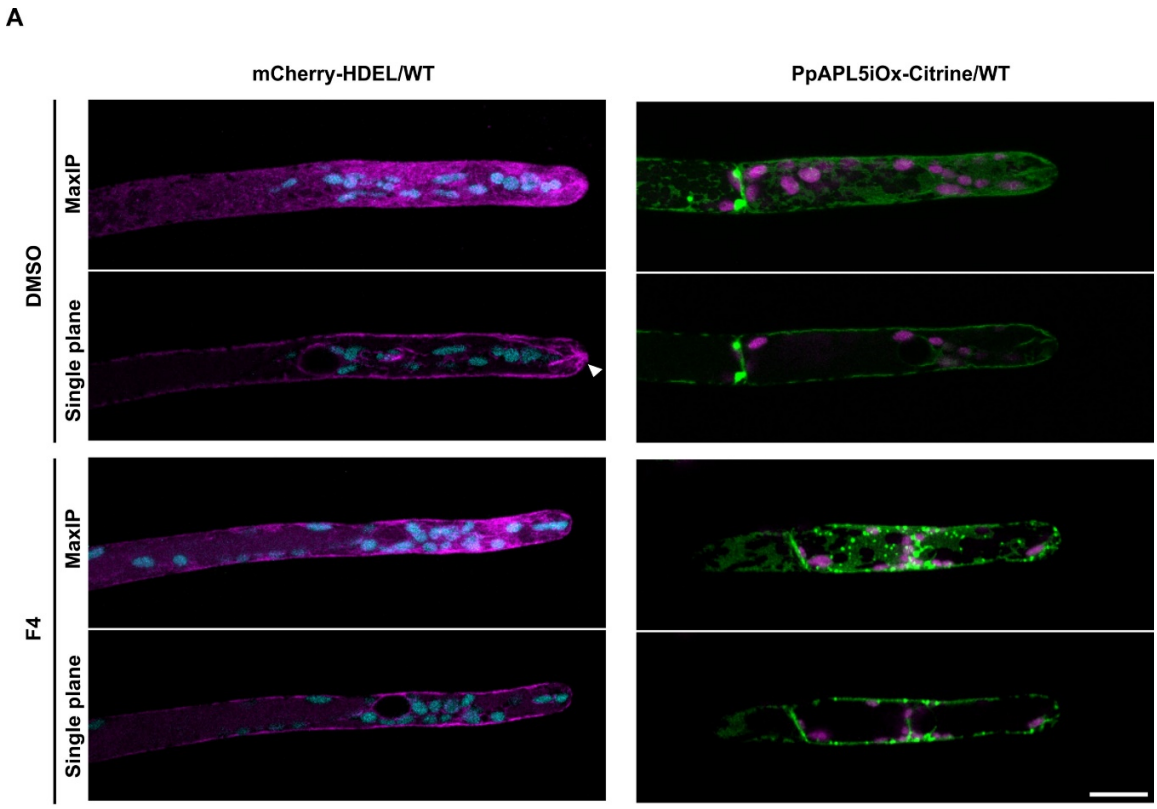

FIGURE 13

Figure 13. PpAPL5 localizes to the endoplasmic reticulum (ER).

A. mCherry-HDEL and PpAPL5iOx-Citrine were induced with 10 nM β-estradiol for 16 hours. mCherry-HDEL was used as an ER marker. An ER scaffold is observed at the tip of the apical cell which is lost upon 100 µM Reagent F4 treatment for 1 hour. 0.1% DMSO was used as control. PpAPL5iOx-Citrine localizes to the ER but seems to induce more ER cisternae, sheet-like structures. Reagent F4 treatment of PpAPL5iOx-Citrine leads to more aggregate formation. Scale bar, 15 µm.

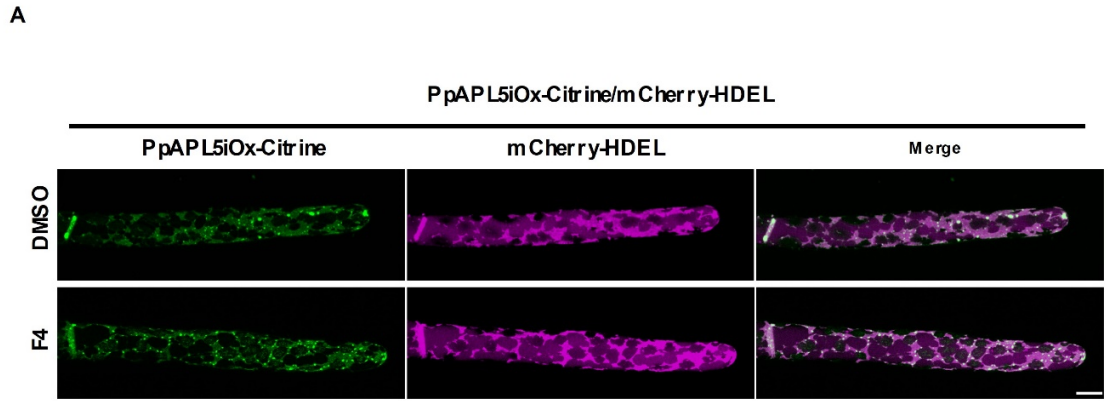

FIGURE 14

Figure 14. PpAPL5 colocalizes with HDEL (ER) marker and causes sheet-like structures in the ER.

A. PpAPL5iOx-Citrine overexpression in the mCherry-HDEL background leads to more ER sheet-like structures. Samples were induced with 10 nM β-estradiol for 16 hours and subsequently treated with 0.1% DMSO (as control) and 100 µM Reagent F4 for one hour and observed. Scale bar, 10 µm.

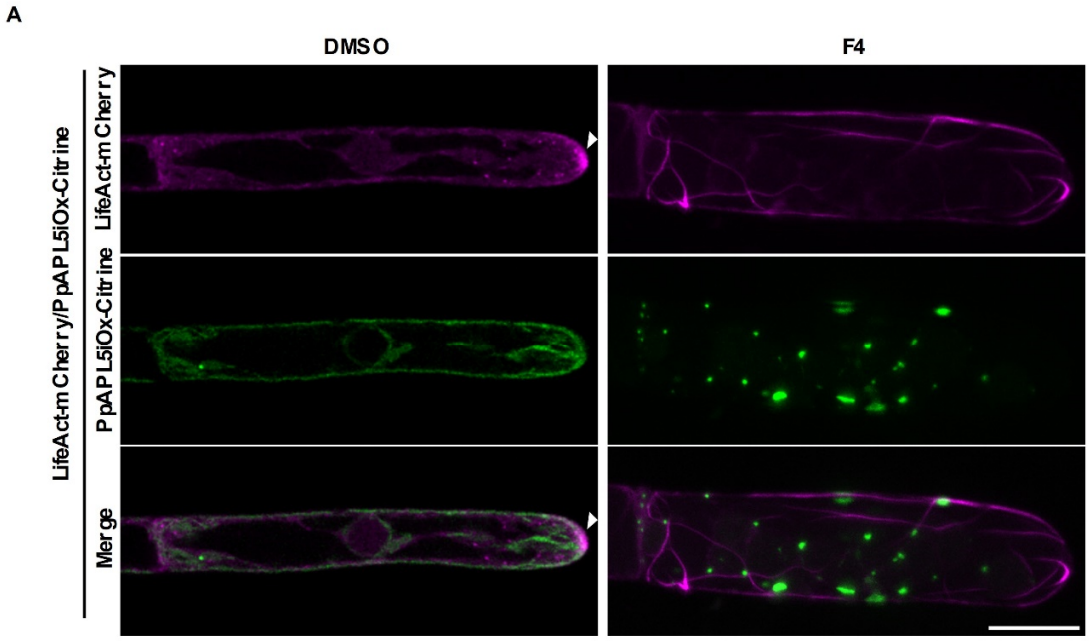

FIGURE 15

858

859 *Figure 15. Effects of Reagent F4 on PpAPL5 overexpression and actin filaments.*

860 A. Single plane confocal images of LifeAct-mCherry in the PpAPL5iOx#21
861 background. Samples were induced with 10 nM β-estradiol for 16 hours. Treatment
862 of samples with Reagent F4 for one hour caused depolymerization of actin and
863 aggregation of PpAPL5 overexpressed protein. There is no clear correlation
864 between the PpAPL5 aggregation and actin depolymerization). 0.1% DMSO was
865 used for control. White arrowheads indicate actin foci. Scale bar, 10 μm.

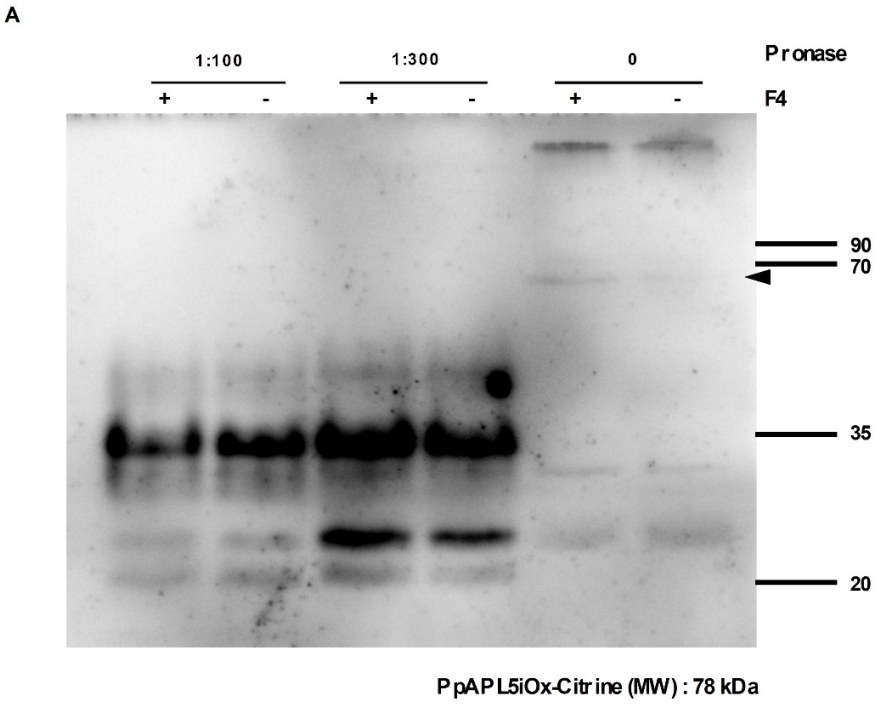

FIGURE 16

Figure 16. DARTS detection of PpAPL5 as Reagent F4's binding target via immunoblotting.

A. Total protein of PpAPL5iOx-Citrine#21 was treated with Reagent F4, followed by incubation with Pronase. PpAPL5iOx-Citrine is not protected by Reagent F4 under Pronase-mediated proteolysis. Black arrowhead marks the PpAPL5iOx-Citrine band.

Acknowledgments

I would like to express my sincerest gratitude to my supervisor, Dr. Tomomichi Fujita, for his continued support and encouragement during my dissertation research. I would also like to thank Drs. Yukako Chiba, Takeo Sato, and Satoshi Naramoto for serving as sub-advisors on the dissertation committee for my degree. I am deeply grateful to my parents and siblings for their affection and continuous support.

I thank the Global Facility Center, Hokkaido University for use of the mass spectrometer; Drs. Takashi Ueda and Mitsuyasu Hasebe for their kind gifts of pENTR-LifeAct-Venus plasmid and the transgenic *P. patens*, respectively; Dr Yuji Hiwatashi for providing the GFP-Tubulin transgenic line; Dr Magdalena Bezanilla for providing the ROP4-swmNG transgenic line; Dr. Junpei Takagi for providing the pGWB701-UBQ10-mCherry-HDEL plasmid; Drs. Minoru Kubo and Mitsuyasu Hasebe for providing the vectors pPGX8 and pT1OG; Dr Teh Ooi Kock and Dr Marcel P. Beier for the insightful and valuable discussions.

This work was supported by the Sasakawa Scientific Research Grant from The Japan Science Society (2023-4044) & MEXT scholarship (Prerna Singh), the Japan Science and Technology Agency, Precursory Research for Embryonic Science and Technology (JPMJPR22D6) and by the MEXT (24H00856) (Satoshi Naramoto). This work's presentation in conferences was supported by BioSystems Science Course Grant for Attending Meeting/Conference in 2022, 2023 and 2024.

References

Afgan, E., Baker, D., van den Beek, M., Blankenberg, D., Bouvier, D., Čech, M., Chilton, J., Clements, D., Coraor, N., Eberhard, C., Grüning, B., Guerler, A., Hillman-Jackson, J., Von Kuster, G., Rasche, E., Soranzo, N., Turaga, N., Taylor, J., Nekrutenko, A., Goecks, J., 2016. The Galaxy platform for accessible, reproducible and collaborative biomedical analyses: 2016 update. Nucleic Acids Res. 44, W3–W10. https://doi.org/10.1093/nar/gkw343

Andrews S, 2010. FastQC a quality control tool for high throughput sequence data [WWW Document]. URL https://www.bioinformatics.babraham.ac.uk/projects/fastqc/ (accessed 12.9.24).

Ashton, N.W., Cove, D.J., 1977. The isolation and preliminary characterisation of auxotrophic and analogue resistant mutants of the moss, Physcomitrella patens. Mol. Gen. Genet. MGG 154, 87–95. https://doi.org/10.1007/BF00265581

Augustine, R.C., Pattavina, K.A., Tüzel, E., Vidali, L., Bezanilla, M., 2011. Actin interacting Protein1 and actin depolymerizing factor drive rapid actin dynamics in physcomitrella patens. Plant Cell 23, 3696–3710. https://doi.org/10.1105/tpc.111.090753

Augustine, R.C., Vidali, L., Kleinman, K.P., Bezanilla, M., 2008. Actin depolymerizing factor is essential for viability in plants, and its phosphoregulation is important for tip growth. Plant J. 54, 863–875. https://doi.org/10.1111/j.1365-313X.2008.03451.x

Bao, L., Inoue, N., Ishikawa, M., Gotoh, E., Teh, O.-K., Higa, T., Morimoto, T., Ginanjar, E.F., Harashima, H., Noda, N., Watahiki, M., Hiwatashi, Y., Sekine, M., Hasebe, M., Wada, M., Fujita, T., 2022. A PSTAIRE-type cyclin-dependent kinase controls light responses in land plants. Sci. Adv. 8, eabk2116. https://doi.org/10.1126/sciadv.abk2116

Bascom, C., Jr, Burkart, G.M., Mallett, D.R., O'Sullivan, J.E., Tomaszewski, A.J., Walsh, K., Bezanilla, M., 2019. Systematic survey of the function of ROP regulators and effectors during tip growth in the moss Physcomitrella patens. J. Exp. Bot. 70, 447–457. https://doi.org/10.1093/jxb/ery376

Bezanilla, M., Gladfelter, A.S., Kovar, D.R., Lee, W.-L., 2015. Cytoskeletal dynamics: A view from the membrane. J. Cell Biol. 209, 329–337. https://doi.org/10.1083/jcb.201502062

Bokman, S.H., Ward, W.W., 1981. Renaturation of Aequorea<math><mtext>Aequorea</mtext></math> green-fluorescent protein. Biochem. Biophys. Res. Commun. 101, 1372–1380. https://doi.org/10.1016/0006-291X(81)91599-0

Borevitz, J.O., Ecker, J.R., 2004. PLANT GENOMICS: the third wave. Annu. Rev. Genomics Hum. Genet. 5, 443–477. https://doi.org/10.1146/annurev.genom.5.061903.180017

Bray, N.L., Pimentel, H., Melsted, P., Pachter, L., 2016. Near-optimal probabilistic RNA-seq quantification. Nat. Biotechnol. 34, 525–527. https://doi.org/10.1038/nbt.3519

Burkart, G.M., Baskin, T.I., Bezanilla, M., 2015. A family of ROP proteins that suppresses actin dynamics, and is essential for polarized growth and cell adhesion. J. Cell Sci. 128, 2553–2564. https://doi.org/10.1242/jcs.172445

Cheng, X., Mwaura, B.W., Chang Stauffer, S.R., Bezanilla, M., 2020. A fully functional ROP fluorescent fusion protein reveals roles for this GTPase in subcellular and tissue-level patterning. Plant Cell 32, 3436–3451. https://doi.org/10.1105/tpc.20.00440

Cox, J., Hein, M.Y., Luber, C.A., Paron, I., Nagaraj, N., Mann, M., 2014. Accurate proteome-wide label-free quantification by delayed normalization and maximal peptide ratio extraction, termed MaxLFQ*. Mol. Cell. Proteomics 13, 2513–2526. https://doi.org/10.1074/mcp.M113.031591

Das, A., Slaughter, B.D., Unruh, J.R., Bradford, W.D., Alexander, R., Rubinstein, B., Li, R., 2012. Flippase-mediated phospholipid asymmetry promotes fast Cdc42 recycling in dynamic maintenance of cell polarity. Nat. Cell Biol. 14, 304–310. https://doi.org/10.1038/ncb2444

Davis, J.A., Pares, R.B., Bernstein, T., McDowell, S.C., Brown, E., Stubrich, J., Rosenberg, A., Cahoon, E.B., Cahoon, R.E., Poulsen, L.R., Palmgren, M., López-Marqués, R.L., Harper, J.F., 2020. The lipid flippases ALA4 and ALA5 play critical roles in cell expansion and plant Growth1 [OPEN]. Plant Physiol. 182, 2111–2125. https://doi.org/10.1104/pp.19.01332

Dong, J., MacAlister, C.A., Bergmann, D.C., 2009. BASL controls asymmetric cell division in arabidopsis. Cell 137, 1320–1330. https://doi.org/10.1016/j.cell.2009.04.018

Drakakaki, G., Robert, S., Szatmari, A.-M., Brown, M.Q., Nagawa, S., Van Damme, D., Leonard, M., Yang, Z., Girke, T., Schmid, S.L., Russinova, E., Friml, J., Raikhel, N.V., Hicks, G.R., 2011. Clusters of bioactive compounds target dynamic endomembrane networks in vivo. Proc. Natl. Acad. Sci. 108, 17850–17855. https://doi.org/10.1073/pnas.1108581108

Eklund, D.M., Svensson, E.M., Kost, B., 2010. Physcomitrella patens: a model to investigate the role of RAC/ROP GTPase signalling in tip growth. J. Exp. Bot. 61, 1917–1937. https://doi.org/10.1093/jxb/erq080

Era, A., Tominaga, M., Ebine, K., Awai, C., Saito, C., Ishizaki, K., Yamato, K.T., Kohchi, T., Nakano, A., Ueda, T., 2009. Application of lifeact reveals F-actin dynamics in arabidopsis thaliana and the liverwort, marchantia polymorpha. Plant Cell Physiol. 50, 1041–1048. https://doi.org/10.1093/pcp/pcp055

Ewels, P., Magnusson, M., Lundin, S., Käller, M., 2016. MultiQC: summarize analysis results for multiple tools and samples in a single report. Bioinformatics 32, 3047–3048. https://doi.org/10.1093/bioinformatics/btw354

977 Finka, A., Schaefer, D.G., Saidi, Y., Goloubinoff, P., Zrÿd, J.-P., 2007. In vivo visualization
978 of F-actin structures during the development of the moss Physcomitrella patens.
979 New Phytol. 174, 63–76. https://doi.org/10.1111/j.1469-8137.2007.01989.x
980 Fu, Y., Li, H., Yang, Z., 2002. The ROP2 GTPase controls the formation of cortical fine F-
981 actin and the early phase of directional cell expansion during arabidopsis
982 organogenesis. Plant Cell 14, 777–794. https://doi.org/10.1105/tpc.001537
983 Fu, Y., Wu, G., Yang, Z., 2001. ROP gtpase–dependent dynamics of tip-localized F-actin
984 controls tip growth in pollen tubes. J. Cell Biol. 152, 1019–1032.
985 https://doi.org/10.1083/jcb.152.5.1019
986 Ge, S.X., Jung, D., Yao, R., 2020. ShinyGO: a graphical gene-set enrichment tool for
987 animals and plants. Bioinformatics 36, 2628–2629.
988 https://doi.org/10.1093/bioinformatics/btz931
989 Ge, S.X., Son, E.W., Yao, R., 2018. iDEP: an integrated web application for differential
990 expression and pathway analysis of RNA-Seq data. BMC Bioinformatics 19, 534.
991 https://doi.org/10.1186/s12859-018-2486-6
992 Gorelova, V., Sprakel, J., Weijers, D., 2021. Plant cell polarity as the nexus of tissue
993 mechanics and morphogenesis. Nat. Plants 7, 1548–1559.
994 https://doi.org/10.1038/s41477-021-01021-w
995 Guo, X., Dong, J., 2022. Protein polarization: Spatiotemporal precisions in cell division and
996 differentiation. Curr. Opin. Plant Biol. 68, 102257.
997 https://doi.org/10.1016/j.pbi.2022.102257
998 Harries, P.A., Pan, A., Quatrano, R.S., 2005. Actin-related Protein2/3 complex component
999 ARPC1 is required for proper cell morphogenesis and polarized cell growth in
1000 physcomitrella patens. Plant Cell 17, 2327–2339.
1001 https://doi.org/10.1105/tpc.105.033266
1002 Hepler, P.K., Vidali, L., Cheung, A.Y., 2001. Polarized cell growth in higher plants. Annu.
1003 Rev. Cell Dev. Biol. 17, 159–187. https://doi.org/10.1146/annurev.cellbio.17.1.159
1004 Higaki, T., 2017. Quantitative evaluation of cytoskeletal organizations by microscopic
1005 image analysis. Plant Morphol. 29, 15–21. https://doi.org/10.5685/plmorphol.29.15
1006 Hiwatashi, Y., Obara, M., Sato, Y., Fujita, T., Murata, T., Hasebe, M., 2008. Kinesins are
1007 indispensable for interdigitation of phragmoplast microtubules in the moss
1008 physcomitrella patens. Plant Cell 20, 3094–3106.
1009 https://doi.org/10.1105/tpc.108.061705
1010 Inzé, D., Veylder, L.D., 2006. Cell cycle regulation in plant Development1. Annu. Rev.
1011 Genet. 40, 77–105. https://doi.org/10.1146/annurev.genet.40.110405.090431
1012 Ito, K., Ren, J., Fujita, T., 2014. Conserved function of Rho-related Rop/RAC GTPase
1013 signaling in regulation of cell polarity in *Physcomitrella patens*. Gene 544, 241–
1014 247. https://doi.org/10.1016/j.gene.2014.04.057
1015 Kamitani, M., Kashima, M., Tezuka, A., Nagano, A.J., 2019. Lasy-Seq: a high-throughput
1016 library preparation method for RNA-Seq and its application in the analysis of plant

responses to fluctuating temperatures. Sci. Rep. 9, 7091. https://doi.org/10.1038/s41598-019-43600-0
Kimata, Y., Yamada, M., Murata, T., Kuwata, K., Sato, A., Suzuki, T., Kurihara, D., Hasebe, M., Higashiyama, T., Ueda, M., 2023. Novel inhibitors of microtubule organization and phragmoplast formation in diverse plant species. Life Sci. Alliance 6. https://doi.org/10.26508/lsa.202201657
Kubo, M., Imai, A., Nishiyama, T., Ishikawa, M., Sato, Y., Kurata, T., Hiwatashi, Y., Reski, R., Hasebe, M., 2013. System for stable β-estradiol-inducible gene expression in the moss physcomitrella patens. PLOS ONE 8, e77356. https://doi.org/10.1371/journal.pone.0077356
Liu, W., Xie, Y., Ma, J., Luo, X., Nie, P., Zuo, Z., Lahrmann, U., Zhao, Q., Zheng, Y., Zhao, Y., Xue, Y., Ren, J., 2015. IBS: an illustrator for the presentation and visualization of biological sequences. Bioinformatics 31, 3359–3361. https://doi.org/10.1093/bioinformatics/btv362
Lomenick, B., Hao, R., Jonai, N., Chin, R.M., Aghajan, M., Warburton, S., Wang, J., Wu, R.P., Gomez, F., Loo, J.A., Wohlschlegel, J.A., Vondriska, T.M., Pelletier, J., Herschman, H.R., Clardy, J., Clarke, C.F., Huang, J., 2009. Target identification using drug affinity responsive target stability (DARTS). Proc. Natl. Acad. Sci. 106, 21984–21989. https://doi.org/10.1073/pnas.0910040106
Love, M.I., Huber, W., Anders, S., 2014. Moderated estimation of fold change and dispersion for RNA-seq data with DESeq2. Genome Biol. 15, 550. https://doi.org/10.1186/s13059-014-0550-8
Madeira, F., Madhusoodanan, N., Lee, J., Eusebi, A., Niewielska, A., Tivey, A.R.N., Lopez, R., Butcher, S., 2024. The EMBL-EBI Job Dispatcher sequence analysis tools framework in 2024. Nucleic Acids Res. 52, W521–W525. https://doi.org/10.1093/nar/gkae241
Martin, M., 2011. Cutadapt removes adapter sequences from high-throughput sequencing reads. EMBnet.journal 17, 10–12. https://doi.org/10.14806/ej.17.1.200
McKinney, J.D., Richard, A., Waller, C., Newman, M.C., Gerberick, F., 2000. The practice of structure activity relationships (SAR) in toxicology. Toxicol. Sci. 56, 8–17. https://doi.org/10.1093/toxsci/56.1.8
Menand, B., Yi, K., Jouannic, S., Hoffmann, L., Ryan, E., Linstead, P., Schaefer, D.G., Dolan, L., 2007. An ancient mechanism controls the development of cells with a rooting function in land plants. Science 316, 1477–1480. https://doi.org/10.1126/science.1142618
Michniewicz, M., Brewer, P.B., Friml, J., 2007. Polar auxin transport and asymmetric auxin distribution. Arab. Book 2007. https://doi.org/10.1199/tab.0108
Müller, A., Guan, C., Gälweiler, L., Tänzler, P., Huijser, P., Marchant, A., Parry, G., Bennett, M., Wisman, E., Palme, K., 1998. AtPIN2 defines a locus of Arabidopsis

for root gravitropism control. EMBO J. 17, 6903–6911. https://doi.org/10.1093/emboj/17.23.6903
Naramoto, S., Hata, Y., Fujita, T., Kyozuka, J., 2022. The bryophytes Physcomitrium patens and Marchantia polymorpha as model systems for studying evolutionary cell and developmental biology in plants. Plant Cell 34, 228–246. https://doi.org/10.1093/plcell/koab218
Nishiyama, T., Hiwatashi, Y., Sakakibara, K., Kato, M., Hasebe, M., 2000. Tagged mutagenesis and gene-trap in the moss, physcomitrella patens by shuttle mutagenesis. DNA Res. 7, 9–17. https://doi.org/10.1093/dnares/7.1.9
Nofer, J.-R., Remaley, A.T., Feuerborn, R., Wolinnéska, I., Engel, T., Eckardstein, A. von, Assmann, G., 2006. Apolipoprotein A-I activates Cdc42 signaling through the ABCA1 transporter. J. Lipid Res. 47, 794–803. https://doi.org/10.1194/jlr.M500502-JLR200
Orr, R.G., Cheng, X., Vidali, L., Bezanilla, M., 2020. Orchestrating cell morphology from the inside out – using polarized cell expansion in plants as a model. Curr. Opin. Cell Biol., Cell Architecture 62, 46–53. https://doi.org/10.1016/j.ceb.2019.08.004
Pai, M.Y., Lomenick, B., Hwang, H., Schiestl, R., McBride, W., Loo, J.A., Huang, J., 2015. Drug Affinity Responsive Target Stability (DARTS) for small-molecule target identification, in: Hempel, J.E., Williams, C.H., Hong, C.C. (Eds.), Chemical Biology: Methods and Protocols. Springer, New York, NY, pp. 287–298. https://doi.org/10.1007/978-1-4939-2269-7_22
Pellegrino, M., Furmaniak-Kazmierczak, E., LeBlanc, J.C., Cho, T., Cao, K., Marcovina, S.M., Boffa, M.B., Côté, G.P., Koschinsky, M.L., 2004. The apolipoprotein(a) component of lipoprotein(a) stimulates actin stress fiber formation and loss of cell-cell contact in cultured endothelial cells*. J. Biol. Chem. 279, 6526–6533. https://doi.org/10.1074/jbc.M309705200
Poulsen, L.R., López-Marqués, R.L., McDowell, S.C., Okkeri, J., Licht, D., Schulz, A., Pomorski, T., Harper, J.F., Palmgren, M.G., 2008. The arabidopsis P4-ATPase ALA3 localizes to the golgi and requires a β-subunit to function in lipid translocation and secretory vesicle formation. Plant Cell 20, 658–676. https://doi.org/10.1105/tpc.107.054767
Rensing, S.A., Goffinet, B., Meyberg, R., Wu, S.-Z., Bezanilla, M., 2020. The moss physcomitrium (physcomitrella) patens: a model organism for non-seed plants[OPEN]. Plant Cell 32, 1361–1376. https://doi.org/10.1105/tpc.19.00828
Ruan, J., Lai, L., Ou, H., Yi, P., 2023. Two subtypes of GTPase-activating proteins coordinate tip growth and cell size regulation in Physcomitrium patens. Nat. Commun. 14, 7084. https://doi.org/10.1038/s41467-023-42879-y
Saarikangas, J., Zhao, H., Lappalainen, P., 2010. Regulation of the actin cytoskeleton-plasma membrane interplay by phosphoinositides. Physiol. Rev. 90, 259–289. https://doi.org/10.1152/physrev.00036.2009

Saavedra, L., Balbi, V., Lerche, J., Mikami, K., Heilmann, I., Sommarin, M., 2011. PIPKs are essential for rhizoid elongation and caulonemal cell development in the moss Physcomitrella patens. Plant J. 67, 635–647. https://doi.org/10.1111/j.1365-313X.2011.04623.x

Saito, K., Fujimura-Kamada, K., Hanamatsu, H., Kato, U., Umeda, M., Kozminski, K.G., Tanaka, K., 2007. Transbilayer phospholipid flipping regulates Cdc42p signaling during polarized cell growth via rga GTPase-activating proteins. Dev. Cell 13, 743–751. https://doi.org/10.1016/j.devcel.2007.09.014

Sakai, Y., Sugano, S.S., Kawase, T., Shirakawa, M., Imai, Y., Kawamoto, Y., Sugiyama, H., Nakagawa, T., Hara-Nishimura, I., Shimada, T., 2017. The chemical compound bubblin induces stomatal mispatterning in Arabidopsis by disrupting the intrinsic polarity of stomatal lineage cells. Development 144, 499–506. https://doi.org/10.1242/dev.145458

Schindelin, J., Arganda-Carreras, I., Frise, E., Kaynig, V., Longair, M., Pietzsch, T., Preibisch, S., Rueden, C., Saalfeld, S., Schmid, B., Tinevez, J.-Y., White, D.J., Hartenstein, V., Eliceiri, K., Tomancak, P., Cardona, A., 2012. Fiji: an open-source platform for biological-image analysis. Nat. Methods 9, 676–682. https://doi.org/10.1038/nmeth.2019

Schreiber, SL., 1998. Chemical genetics resulting from a passion for synthetic organic chemistry. Bioorg Med Chem. https://doi.org/10.1016/s0968-0896(98)00126-6. PMID: 9784856.

Settleman, J., 2005. Intercalating arabidopsis leaf cells: a jigsaw puzzle of lobes, necks, ROPs, and RICs. Cell 120, 570–572. https://doi.org/10.1016/j.cell.2005.02.025

Smaczniak, C., Li, N., Boeren, S., America, T., van Dongen, W., Goerdayal, S.S., de Vries, S., Angenent, G.C., Kaufmann, K., 2012. Proteomics-based identification of low-abundance signaling and regulatory protein complexes in native plant tissues. Nat. Protoc. 7, 2144–2158. https://doi.org/10.1038/nprot.2012.129

Soneson, C., Love, M.I., Robinson, M.D., 2016. Differential analyses for RNA-seq: transcript-level estimates improve gene-level inferences. https://doi.org/10.12688/f1000research.7563.1

Takano, J., Tanaka, M., Toyoda, A., Miwa, K., Kasai, K., Fuji, K., Onouchi, H., Naito, S., Fujiwara, T., 2010. Polar localization and degradation of Arabidopsis boron transporters through distinct trafficking pathways. Proc. Natl. Acad. Sci. 107, 5220–5225. https://doi.org/10.1073/pnas.0910744107

Tamura, K., Stecher, G., Kumar, S., 2021. MEGA11: Molecular Evolutionary Genetics Analysis Version 11. Mol. Biol. Evol. 38, 3022–3027. https://doi.org/10.1093/molbev/msab120

Tang, D., Chen, M., Huang, X., Zhang, Guicheng, Zeng, L., Zhang, Guangsen, Wu, S., Wang, Y., 2023. SRplot: A free online platform for data visualization and graphing. PLOS ONE 18, e0294236. https://doi.org/10.1371/journal.pone.0294236

Vidali, L., Augustine, R.C., Kleinman, K.P., Bezanilla, M., 2007. Profilin is essential for tip growth in the moss physcomitrella patens. Plant Cell 19, 3705–3722. https://doi.org/10.1105/tpc.107.053413

Vidali, L., van Gisbergen, P.A.C., Guérin, C., Franco, P., Li, M., Burkart, G.M., Augustine, R.C., Blanchoin, L., Bezanilla, M., 2009. Rapid formin-mediated actin-filament elongation is essential for polarized plant cell growth. Proc. Natl. Acad. Sci. 106, 13341–13346. https://doi.org/10.1073/pnas.0901170106

Waterhouse, A.M., Procter, J.B., Martin, D.M.A., Clamp, M., Barton, G.J., 2009. Jalview Version 2—a multiple sequence alignment editor and analysis workbench. Bioinformatics 25, 1189–1191. https://doi.org/10.1093/bioinformatics/btp033

Wu, S.-Z., Bezanilla, M., 2018a. Actin and microtubule cross talk mediates persistent polarized growth. J. Cell Biol. 217, 3531–3544. https://doi.org/10.1083/jcb.201802039

Wu, S.-Z., Bezanilla, M., 2018b. Actin and microtubule cross talk mediates persistent polarized growth. J. Cell Biol. 217, 3531–3544. https://doi.org/10.1083/jcb.201802039

Yamada, M., Goshima, G., 2018. The KCH kinesin drives nuclear transport and cytoskeletal coalescence to promote tip cell growth in physcomitrella patens. Plant Cell 30, 1496–1510. https://doi.org/10.1105/tpc.18.00038

Yang, Y., Niu, Y., Chen, T., Zhang, H., Zhang, J., Qian, D., Bi, M., Fan, Y., An, L., Xiang, Y., 2022a. The phospholipid flippase ALA3 regulates pollen tube growth and guidance in Arabidopsis. Plant Cell 34, 3718–3736. https://doi.org/10.1093/plcell/koac208

Yang, Y., Niu, Y., Chen, T., Zhang, H., Zhang, J., Qian, D., Bi, M., Fan, Y., An, L., Xiang, Y., 2022b. The phospholipid flippase ALA3 regulates pollen tube growth and guidance in Arabidopsis. Plant Cell 34, 3718–3736. https://doi.org/10.1093/plcell/koac208

Ye, Z.-H., Zhong, R., 2022. Cell wall biology of the moss Physcomitrium patens. J. Exp. Bot. 73, 4440–4453. https://doi.org/10.1093/jxb/erac122

Yi, P., Goshima, G., 2020. Rho of Plants GTPases and Cytoskeletal Elements Control Nuclear Positioning and Asymmetric Cell Division during Physcomitrella patens Branching. Curr. Biol. 30, 2860-2868.e3. https://doi.org/10.1016/j.cub.2020.05.022

Zhang, X., Adamowski, M., Marhava, P., Tan, S., Zhang, Y., Rodriguez, L., Zwiewka, M., Pukyšová, V., Sánchez, A.S., Raxwal, V.K., Hardtke, C.S., Nodzyński, T., Friml, J., 2020. Arabidopsis flippases cooperate with arf gtpase exchange factors to regulate the trafficking and polarity of pin auxin transporters[open]. Plant Cell 32, 1644–1664. https://doi.org/10.1105/tpc.19.00869

Zhou, Y., Yang, Y., Niu, Y., Fan, T., Qian, D., Luo, C., Shi, Y., Li, S., An, L., Xiang, Y., 2020. The tip-localized phosphatidylserine established by arabidopsis Ala3 is

crucial for rab gtpase-mediated vesicle trafficking and pollen tube growth. Plant Cell 32, 3170–3187. https://doi.org/10.1105/tpc.19.00844

Supplementary Information

Supplementary Movie 1 – FRAP analysis of ROP4-swmNG under the effect of Reagent F4.

Supplementary Table S1 – Differential gene expression analysis of *P. patens* treated with Reagent F4.

Supplementary Table S2 – GO term enrichment analysis of upregulated and downregulated DEGs of *P. patens* treated with Reagent F4.

Supplementary Table S3 – Peptide abundances quantified post LC-MS/MS data analysis in mock and 100 μM F4 treated samples after Pronase proteolysis.

Supplementary Table S4 – List of primers used in this study.

Table S4

Sequence (5'- 3')	Description
AACCAATTCAGTCGACATGAAGGTACAGGAGGGT	5' primer for HDEL marker line cloning
AAGCTGGGTCTAGATATCCTTACAGCTCGTCATGAGATCTCTT	3' primer for HDEL marker line cloning
AACCAATTCAGTCGACATGACTAAGATGGCATTGCGAAG	5' primer for pENTR1A-PpAPL5 cloning
AAGCTGGGTCTAGATATCCTTTCCCCTGCTTGATATCAGCTGC	3' primer pENTR1A-PpAPL5 cloning